HAL open science

Early Pleistocene Orbital-Scale Variability in Australian Northwest Shelf Sediments

Song Zhao, Katharine M Grant, David Heslop, Stephen J Gallagher, Clara T Bolton, Gerald Auer

To cite this version:

Song Zhao, Katharine M Grant, David Heslop, Stephen J Gallagher, Clara T Bolton, et al.. Early Pleistocene Orbital-Scale Variability in Australian Northwest Shelf Sediments. Paleoceanography and Paleoclimatology, 2024, 39 (10), pp.e2024PA005015. ⟨10.1029/2024PA005015⟩. ⟨hal-04745904⟩

HAL Id: hal-04745904

https://hal.science/hal-04745904v1

Submitted on 21 Oct 2024

HAL is a multi-disciplinary open access archive for the deposit and dissemination of scientific research documents, whether they are published or not. The documents may come from teaching and research institutions in France or abroad, or from public or private research centers.

L'archive ouverte pluridisciplinaire **HAL**, est destinée au dépôt et à la diffusion de documents scientifiques de niveau recherche, publiés ou non, émanant des établissements d'enseignement et de recherche français ou étrangers, des laboratoires publics ou privés.

Autorisation HAL

HAL Authorization

Citation:
Zhao, S., Grant, K. M., Heslop, D., Gallagher, S. J., Bolton, C. T., & Auer, G. (2024). Early Pleistocene orbital-scale variability in Australian Northwest Shelf sediments. *Paleoceanography and Paleoclimatology*, *39*, e2024PA005015. https://doi.org/10.1029/2024PA005015

manuscript submitted to *Paleoceanography and Paleoclimatology*

Received 6 SEP 2024
Accepted 9 OCT 2024

Early Pleistocene orbital-scale variability in Australian Northwest Shelf sediments

Song Zhao[1,2*], Katharine M. Grant[1], David Heslop[1], Stephen J. Gallagher[3], Clara T. Bolton[4], and Gerald Auer[5]

[1] Research School of Earth Sciences, Australian National University, Canberra, ACT, Australia.

[2] State Key Laboratory of Isotope Geochemistry and CAS Center for Excellence in Deep Earth Science, Guangzhou Institute of Geochemistry, Chinese Academy of Sciences, Guangzhou, China.

[3] School of Geography, Earth and Atmospheric Sciences, University of Melbourne, Melbourne, Victoria, Australia.

[4] Aix-Marseille University, CNRS, IRD, INRAE, CEREGE, Aix-en-Provence, France.

[5] University of Graz, Department of Earth Sciences, NAWI Graz Geocenter, Graz, Austria.

*Corresponding author: Song Zhao (zhaosong@gig.ac.cn)

Key Points:

- This study establishes a new orbitally-constrained chronology for IODP Site U1464.
- Australian Northwest shelf sediments preserve ~400 kyr eccentricity cycles in %$CaCO_3$ and ~41 kyr obliquity cycles in dust proxy records.
- Obliquity in Northwest Australian dust flux may be related to the East Asian winter monsoon and summer inter-tropical insolation gradient.

Abstract

Paleoclimate proxy records from regions sensitive to humidity/aridity extremes provide crucial insights into the natural forcing mechanisms underlying long-term climate variability in broader regions. One such area is Northwest Australia, where the Australian monsoon impacts its northernmost fringes, which are bordered by the Great Sandy Desert inland. Marine sediments from the Australian Northwest Shelf record fluvial run-off and eolian dust input during the wet and dry seasons, respectively. The location is therefore ideal for investigating long-term variability in the Australian monsoon and Northwest Australian dust flux over orbital timescales. However, there are few continuous, high-resolution paleoclimate records from this region spanning the early Pleistocene, when strong ice-climate feedbacks of the late Pleistocene did not yet dominate global climate. Here, we present geochemical and environmental magnetic proxy records that reveal %$CaCO_3$ and dust-flux variability between 2.9 and 1.6 million years (Myr) ago from International Ocean Discovery Program Expedition 356 Site U1464 on the Australian Northwest Shelf. We establish a new, orbitally-tuned chronology for Site U1464, primarily based on ~400 thousand year (kyr) eccentricity cyclicity in %$CaCO_3$, and observe strong obliquity variability (41 kyr and 54 kyr periodicities) but almost no precession signal in the dust-flux records. We propose that the 41 kyr cycle in Northwest Australian dust flux could be a linear response to East Asian winter monsoon intensity and/or the summer inter-tropical insolation gradient, whereas the 54 kyr cyclicity might be a non-linear response to obliquity amplitude modulation via the summer inter-tropical insolation gradient effect on the cross-equatorial atmospheric circulations.

1. Introduction

Sediments from the Australian Northwest Shelf (NWS) serve as a valuable archive of past Australian monsoon variability and dust flux from the Australian interior. Fluvial transport of terrigenous materials to the NWS occurs during the wet season (December to March), primarily from the Ord and Fitzroy Rivers in the far north, and from the De Grey and Fortescue Rivers at the southern margin (Australia's River Basins, 1997) (Figure 1, Figure S1). In contrast, eolian dust flux to the NWS primarily takes place from austral spring to autumn (September to May), driven by frontal systems and southeasterly trade winds transporting dust from Lake Eyre Basin across Northwest Australia (Baddock et al., 2015; Ekström et al., 2004; Gallagher & deMenocal,

2019; McGowan & Clark, 2008; McTainsh, 1989; Strong et al., 2011). These seasonal patterns of precipitation and dust flux are therefore closely tied to changes in insolation and the latitudinal position of the Intertropical Convergence Zone (ITCZ), as modern observations indicate a strong coupling between seasonal migrations of insolation maxima, the ITCZ, rainfall, and southeasterly trade winds in Northwest Australia (Suppiah, 1992). However, over longer timescales, the relationship between insolation/orbital forcing and Australian monsoon/dust-flux variability remains poorly understood. Australian monsoon strength has been suggested to respond to local insolation dominated by precession (Holbourn et al., 2005; Liu et al., 2015; Pei et al., 2021) or to Northern Hemisphere insolation driven by precession and obliquity (Magee et al., 2004). These varying responses of the Australian monsoon to orbital forcing could, at least in part, be attributed to glacial fluctuations. For example, many studies have reported evidence of increased dust flux to the Australian NWS (Courtillat et al., 2020; Hesse et al., 2004; Pei et al., 2021; Stuut et al., 2014, 2019) and decreased Australian monsoonal precipitation (Gallagher et al., 2014; Gallagher & Wagstaff, 2021; Kershaw et al., 2003; Magee et al., 2004; Miller et al., 2018; Stuut et al., 2014, 2019) during glacials and/or stadials, while other studies have inferred intensified Australian monsoonal precipitation during glacials and/or stadials in response to southward migration of the ITCZ (Bayon et al., 2017; Denniston et al., 2017; Fu et al., 2017). Therefore, a long record during less glaciated periods could help clarify the role of insolation/orbital forcing in Australian monsoon and dust flux variability.

A significant barrier is the scarcity of continuous, high-resolution paleoclimate records from this region spanning >1 million years (Myr), especially ones extending back to the early Pleistocene when the ice-climate feedback was not strong. Of the available high-resolution records, most tend to be focused on the last glacial cycle (the last ~130 kyr), when the effects of millennial-scale climate variability and/or the last deglaciation obfuscate the primary response of the Australian monsoon and Northwest Australian dust flux to direct orbital forcing (Bayon et al., 2017; Denniston et al., 2017; Fu et al., 2017; Miller et al., 2018). A few longer records (>1 Myr) do exist, but their interpretations typically emphasize long-term trends (Christensen et al., 2017; Stuut et al., 2019). For example, proxy records of past dust flux based on sedimentary Th/K at International Ocean Discovery Program (IODP) Site U1463 (Christensen et al., 2017) and Log(Zr/Fe) at Ocean Drilling Program (ODP) Site 762 (Stuut et al., 2019) reveal increasing aridity variance from the Pliocene to the Pleistocene.

Modelling studies on Australian monsoon variability over orbital timescales are relatively rare. Earlier studies suggested a direct response of Australian summer monsoon precipitation to local insolation (Chappell & Syktus, 1996; Wyrwoll & Valdes, 2003; Wyrwoll et al., 2007), or to Northern Hemisphere insolation via cross-equatorial flow (Miller et al., 2005), but these simulations were limited by modelling capacity at that time, such as low-resolution grids and a lack of some important feedback processes. More recent model simulations suggest that obliquity plays a greater role than expected given its smaller contribution to insolation changes relative to precession, and that higher obliquity could result in stronger summer monsoons in Northwest Australia via a stronger pressure gradient between intensified Siberian High and Australian Low pressure cells (Liu et al., 2015; Shi et al., 2011; Wyrwoll et al., 2007). This obliquity-monsoon relationship in simulations, however, conflicts with recent proxy observations of monsoonal precipitation in Northwest Australia (Zhang et al., 2020; 2022) and previous understandings of East Asian winter monsoon (EAWM) dynamics (Ding et al., 2002; Sun et al., 2006).

We have generated continuous, high-resolution proxy records of Northwest Australian dust flux based on scanning X-ray fluorescence (XRF) and environmental magnetism data from IODP Site U1464 (Australian NWS) spanning the last 2.9 Myr. The records show strong cyclic variability between 2.9 and 1.6 Ma, followed by a marked transition to weaker geochemical and magnetic signals in the mid to late Pleistocene. We therefore focus on the 2.9-1.6 Ma time interval, corresponding to the widespread expansion of Northern Hemisphere and Antarctic ice sheets, strengthening latitudinal temperature gradients, and subsequent repositioning of wind bands (Bailey et al., 2013; Brierley & Fedorov, 2010; Clark et al., 1999; Ganopolski et al., 1998; Mudelsee & Raymo, 2005). Nonetheless, this time interval pre-dates the Mid-Pleistocene Transition (MPT), when the amplitude of glacial-interglacial cycles and attendant ice-climate feedbacks increased. Thus, our records capture dust-flux variability in the Australian monsoon region in detail over multiple orbital cycles during a time of gradual global climate change, prior to the onset of strong ice-climate feedbacks which have been shown to interfere with insolation/orbital forcing of monsoon and dust flux variability.

Accurate dating of sediment sequences from the Australian NWS over the Plio-Pleistocene has proven to be problematic due to biostratigraphic diachroneity (Groeneveld et al., 2021), magnetostratigraphic ambiguity (Gallagher et al., 2017a; 2017b), and a lack of robust oxygen

isotope stratigraphy (Groeneveld et al., 2021). Nonetheless, recent studies have established a revised chronological framework for nearby ODP Site 762 and IODP Site U1463 by combining orbital tuning of paleoclimate records with biostratigraphic age constraints (Auer et al., 2020; Groeneveld et al., 2021). While these studies incorporated the tuning of benthic $\delta^{13}C$ and/or $\delta^{18}O$ records, it remained challenging to reconstruct a robust Plio-Pleistocene chronology with no ambiguity. In this study, we present a new, alternative, orbitally-tuned chronology for IODP Site U1464 by using the strong eccentricity and obliquity signals in our %$CaCO_3$ and Log(Zr/Rb) records for tuning. Finally, we explore potential drivers of the orbital-scale variability detected in the %$CaCO_3$ and dust-flux proxy records at Site U1464.

2. Materials and Methods

2.1. Site Location & Sampling

We utilized marine sediments from IODP Site U1464 (18°03.9′S 118°37.9′E, 264 m water depth, Figure 1), cored during IODP Expedition 356 (Gallagher et al., 2017a). This site is located on the central Australian NWS at the southern edge of the modern Australian monsoon region (Figure 1), and lies in the main pathway of eolian dust flux from Northwest Australia that is transported by southeasterly trade winds (Bowler, 1976; Gallagher & deMenocal, 2019) (Figure S1). Site U1464 is thus optimally positioned to study eolian flux from Northwest Australia. A suite of 80 u-channels (each measuring 150 x 2 x 2 cm) was sampled at Kochi Core Center, Japan, in January 2019, from continuous core sections spanning the upper 108.2 m of Hole U1464D. Following non-destructive analyses (see below), the u-channels were sub-sampled every 1 cm downcore into ‘cube’ sub-samples of ~4 cm^3 (1 x 2 x 2 cm) for further analyses.

2.2. Scanning X-ray fluorescence (XRF)

All of the Site U1464 u-channels were scanned at 0.5-cm resolution at the Research School of Earth Sciences (RSES), Australian National University (ANU), Canberra, using a third-generation Avaatech XRF core scanner. Each u-channel was covered with 4 µm-thick Ultralene film prior to measurement, and then measured at 10 kV with a 0.5 mA current and no filter, 30 kV with a 0.5 mA current and Pd-thin filter, and 50 kV with a 0.6 mA current and Cu filter. Count times of 30 s, 20 s and 10 s were used for these three runs, respectively, and three replicate measurements were taken every 75 cm to check reproducibility. Element spectra were processed

into element counts using WinAxil software, and reliable element data were obtained for Ca, Sr, Fe, Ti, Zr, Rb, Si, Cl, Br and S. 141 replicate samples were measured three times for estimation of uncertainties, and precisions were calculated as the ratio of the standard deviation to the measured value expressed as a percentage. Precisions for Ca, Sr, Fe, Ti, Zr, Rb, Si, Cl, Br and S counts in the studied interval were 0.2 %, 0.4 %, 0.7 %, 4.7 %, 3.3 %, 10.2 %, 1.0 %, 1.0 %, 3.4 % and 3.5 %, respectively.

2.3. XRF Calibration

To convert the scanning XRF 'counts' into element concentrations, 50 of the cube subsamples were chosen to cover a range of lithologies (based on the XRF scan results) and depth intervals. Approximately 0.2 g of each cube sample was oven-dried and ground with an agate mortar and pestle. Sediment powder samples were soaked and extracted using 2 ml of nitric acid and 1 ml of hydrochloric acid, and the supernatant was diluted for analysis. Single element concentrations were determined using an Inductively Coupled Plasma Optical Emission Spectrometer (ICP-OES) 5110 by Agilent at the RSES, ANU. High-quality control of the ICP-OES measurements was based on 10 certified reference materials (marine sediments BCSS-1, MESS-1 and estuarine sediments 1646). Ca, Sr, Fe and Ti concentrations were well above detection limits for this method, however the Ca measurements show extremely low precision (Table S1). Additionally, all of the blank samples used during the analyses revealed Ca contamination, probably because Ca is a common element in the laboratories, resulting in the very low measurement precision for Ca. Other XRF elements (especially Zr and Rb) are not calibrated, because OES-derived concentrations of these elements were not produced for this study.

The Ca, Sr, Ti and Fe ICP-OES concentrations were used to convert Ca, Sr, Ti and Fe XRF counts into concentrations using a multivariate log-ratio calibration, following Weltje et al. (2015). This calibration method is more reliable than a basic univariate calibration (i.e., that based on element-by-element regressions), which does not account for physical constraints on compositional data and matrix effects due to the presence of other elements (Weltje et al., 2015). An undefined variable is included in our calibration and is here termed 'everything else', hence the relative concentrations of elements Ca, Sr, Ti, Fe and 'everything else' sum to 100%. The predictive power of our calibration has been assessed by cross-plotting the reference with the predicted concentrations (Figure S2). High r^2 values for Sr (0.91), Ti (0.78) and Fe (0.92)

indicate a robust calibration. The low OES precision and low r^2 (0.27) value for Ca suggest that the OES-derived Ca and Ca calibration are not reliable. We therefore use the relationship between our ln(Ca/Fe) data and shipboard %$CaCO_3$ measurements (r^2=0.90) to convert our scanning XRF ln(Ca/Fe) record into estimated $CaCO_3$ content (Table S2, Figure S2f), following Liebrand et al. (2016).

To further validate the robustness of trends in the %$CaCO_3$ record described above, the centred log-ratio (clr) of Ca counts was calculated based on Weltje et al. (2015):

$$\mathrm{clr}(X) = [\ln(x_1)-\ln(g), \ldots\ldots, \ln(x_j)-\ln(g), \ldots\ldots, \ln(x_D)-\ln(g)] \qquad (1)$$

where X is the composition matrix comprising D elements, and ln(g) = (1/D) * $\sum_{j=1}^{D} \ln(x_j)$. In this study, X represents a ten-element matrix (Ca, Sr, Fe, Ti, Zr, Rb, Si, Cl, Br and S) and D is 10. The major advantage of clr(Ca) over Ca counts is that the clr(Ca) can remove the specimen effect in XRF scanning to some extent, for example effects due to grain-size distribution, the irregular surface of a split core, variable water and organic content, and thickness of an adhesive pore-water film covering the split core surface (Weltje et al., 2015). Additionally, the clr transformation is less affected by variations of terrigenous elements in a sample (the so-called dilution effect) than single element counts. The impact of the clr transformation is illustrated for Ca and Sr counts at Site U1464 (Figure S3c-h), and the good agreement of trends and cycles between clr(Ca) and calibrated %$CaCO_3$ suggests that our $CaCO_3$ calibration method is reliable (Figure S3c-d; Figure S4a and S4e; Figure S5a-b and S5f-g).

2.4. Environmental magnetism

Magnetic properties were measured on all u-channels at 1-cm intervals using a 2-G Enterprises Model 760 cryogenic magnetometer at the Black Mountain Paleomagnetism Laboratory, ANU. For each u-channel, an anhysteretic remanent magnetization (ARM) was imparted in an alternating field (AF) of 100 mT with a superimposed 0.05 mT bias field and then AF demagnetized in 13 steps from 5 mT to 170 mT. Next, an isothermal remanent magnetization (IRM) was imparted in a 1 T field, which was demagnetized in 13 stepwise AFs from 5 mT to 170 mT. The first/last four measurements of each parameter for every u-channel (topmost and lowest 4 cm) were discarded to avoid edge effects impacting the resultant ARM and IRM records.

2.5. Mass accumulation rate

Mass accumulation rates (MARs) were calculated for $CaCO_3$, Sr, Ti and Fe using the following:

$$\text{MAR (g/cm}^2\text{/kyr)} = \text{Elemental Proportion ([0-1])} \times \text{SRs (cm/kyr)} \times \text{DBD (g/cm}^3\text{)} \qquad (2)$$

where SR is linearly interpolated sedimentation rate; DBD is dry bulk density, calculated by DBD = (1-Theta) × grain density; Theta is fractional porosity, calculated using Theta = (GRA - grain density) / (1 - grain density); GRA is gamma-ray attenuation, which can be considered as wet bulk density. The GRA and grain density data are from shipboard measurements, and the calculated DBD is further verified using discrete DBD measurements from shipboard analyses (Gallagher et al., 2017a).

2.6. Component-free calculations

Component-free calculations can permit evaluation of the extent to which dilution by one sediment constituent is driving long-term trends of another constituent in our records. "$CaCO_3$-free" terrigenous elemental (here Fe and Ti) and "terrigenous-free" carbonate elemental (here Sr) concentrations were calculated based on [terrigenous element] / (1- [$CaCO_3$]) and [Sr] / [$CaCO_3$], respectively, where [$CaCO_3$] ranges from 0 to 1. Similarly, "$CaCO_3$-free" IRM remaining after AF demagnetization at 170 mT ($IRM_{1T@AF\ 170mT}$) was calculated based on the following formula: $CaCO_3$-free $IRM_{1T@AF\ 170mT}$ = [$IRM_{1T@AF\ 170mT}$] / (1- [$CaCO_3$]), where [$CaCO_3$] ranges from 0 to 1.

2.7. Spectral analysis

Power spectra were computed using the REDFIT 3.8c (Schulz & Mudelsee, 2002) and cross-checked using the Multitaper method to investigate the cyclicity of our time series (Thomson, 1982). Data were binned (averages in contiguous 0.3 kyr segments) to retain as much information as possible. Additionally, cross-wavelets were performed to investigate the phase relationship and time evolution of periodicities in specific records (with data averaged in 1 kyr bins before analysis) (Grinsted et al., 2004).

3. Chronology

3.1. Bayesian age-depth model based on biostratigraphy

An initial chronology was developed for the upper ~126 m of IODP Site U1464 based on shipboard biostratigraphy. For this, nineteen age control points (Table S3) were used to construct a Bayesian age-depth model using the "Bacon" package (Blaauw & Christen, 2011) (Figure 2a). Cumulative depths below seafloor (CSF-A) for Holes U1464B and U1464D were converted to composite splice depths (CCSF-A) before modelling, based on the established linear relationship between CSF-A and CCSF-A (Gallagher et al., 2017a), and a lithologic boundary was imposed in the model at 43 m CSF-A (= 44.87 m CCSF-A), based on the Unit II/I transition in Hole U1464D (Gallagher et al., 2017a). Age uncertainties of the U1464 biostratigraphic datums are mainly from Backman et al. (2012), Wade et al. (2011) and Gallagher et al. (2017a), and all datums are close to or within the 99% probability interval of our Bacon age-depth model. The last occurrence of *G. ruber* (pink) was identified in this study and its age given by Thompson et al. (1979) is also consistent with our age model (Figure 2a).

3.2. Refined age-depth model based on orbital tunings

Below ~47 m CSF-A, where geochemical signals are strong and unambiguous, we provide additional age controls using our XRF records (Figure 3) via orbital tuning. Power spectra reveal significant eccentricity cyclicity for %$CaCO_3$ (see Section 3.2.1) and obliquity cyclicity for Log(Zr/Rb) (see Section 3.2.2). Therefore, we focused first on tuning Site U1464 %$CaCO_3$, followed by further fine-tuning using Log(Zr/Rb). Finally, we re-ran the Bacon age model using all age constraints with their uncertainties (see Section 3.3), yielding a new orbitally-constrained, statistically evaluated chronology for Site U1464.

3.2.1. $CaCO_3$ tuning at eccentricity 400 kyr band

Spectral analysis revealed significant cyclicity at 0.07 cycles/m for the %$CaCO_3$ record on the depth scale (Figure S4a). Similarly, spectral analysis of the %$CaCO_3$ record on the Bayesian biostratigraphic age model revealed significant power at frequencies of ~0.0024 kyr^{-1}, equivalent to ~400 kyr periodicity (Figure S4e; Figure S5a, S5f). The interpretation and possible drivers of ~400 kyr eccentricity cyclicity in the Site U1464 %$CaCO_3$ are discussed in Section 4.1.

Eccentricity minima, periods when Earth's orbit around the sun was quasi-circular, are shorter in duration than eccentricity maxima, making them more precise age tie-points. Comparison of Site U1464 %$CaCO_3$ on the Bayesian biostratigraphic age model with eccentricity shows that $CaCO_3$ maxima tend to occur during (400 kyr) eccentricity minima (Figure 4), consistent with previous studies (Beaufort et al., 2021; Kochhann et al., 2016; Liebrand et al., 2016; Rickaby et al., 2007). Additional graphic evidence for anti-phasing between Site U1464 %$CaCO_3$ and eccentricity is the cycle-shape of %$CaCO_3$ variations, which display broad troughs and narrow peaks, i.e., consistent pacing with the inverse of the 400 kyr eccentricity cycle (Figure 4). In addition, the 400 kyr periodicity has previously been observed and used as a tuning target for paleoclimate records from adjacent IODP Site U1463 (Figure 1) (Christensen et al., 2017; De Vleeschouwer et al., 2018; Groeneveld et al., 2021). The Site U1464 chronology was therefore further constrained using four tie-points between eccentricity minima and $CaCO_3$ maxima, after exploring different tuning options (Figure S6; Table S4; Supporting Information Text S1). These tie-points all fall within the 99% confidence intervals of the Site U1464 Bayesian biostratigraphy age model (Figure 2a).

3.2.2. Log(Zr/Rb) tuning at obliquity 41 kyr band

Spectral analyses of the rescaled records after eccentricity tuning revealed significant power in Log(Zr/Rb), Log(Zr/Fe) and $IRM_{1T@AF\ 170mT}$ in the ~0.024 kyr^{-1} frequency band (equivalent to ~41 kyr periodicity, Figure S5). Several studies have used Zr as a dust proxy in sediments offshore Northwest Australia (Pei et al., 2021; Stuut et al., 2014, 2019), as windblown heavy/coarse minerals (e.g., $ZrSiO_4$) are enriched in Zr. Conversely, Rb and Fe are preferentially incorporated into riverine fine-grained clays (Pei et al., 2021; Rothwell & Croudace, 2015; Stuut et al., 2014, 2019), thus Log(Zr/Rb) and Log (Zr/Fe) likely reflect the relative contribution of eolian versus fluvial sedimentary components (see Section 4.2 for further discussion). Bandpass filtering of Log(Zr/Rb) at 0.023-0.027 kyr^{-1} frequencies reveals higher values (increased eolian contribution) during obliquity maxima (Figure 5). Recent studies observed an inverse relationship between Australian summer monsoon precipitation proxies (local surface seawater $\delta^{18}O$ and ln(K/Ca) at IODP Site U1483) and obliquity during the late Pleistocene (Zhang et al., 2020; 2022), where higher obliquity was associated with less precipitation (hence less vegetation cover and more erodible particles) and *vice versa*. Similarly, a model-based investigation of obliquity forcing suggested stronger southeasterly trade winds during higher obliquity (Bosmans

et al., 2015); such a scenario would favour transport of dust particles from Northwest Australia to Site U1464. Based on this obliquity-dust relationship and the close phasing of obliquity with our filtered Log(Zr/Rb) record, we further constrain Site U1464 chronology by adding 32 additional tie-points between obliquity minima and minima in filtered Log(Zr/Rb) (Figure 5; Table S5; Figure 2a).

3.3. Refined Bayesian chronology based on biostratigraphy and orbital tunings

To consider potential uncertainties of all age constraints, we re-ran the Bacon age model using the 55 age-depth tie points, including 17 biostratigraphic tie points, 4 eccentricity tuning tie points, 32 obliquity tuning tie points, the last occurrence of *G. ruber* (pink) (newly identified in this study), and the modern age at the seafloor. This refined Bayesian age model accounts for most of the age constraints within its 99.99% confidence interval, with the exception of four biostratigraphic datums (Figure 2b). It is important to note that the shipboard biostratigraphic age constraints at Site U1464 are based on relatively low sampling resolution (generally one sample per core, every 9-10 m). This results in a relatively large degree of freedom for the biostratigraphic tie points within a Bayesian chronology. Additionally, the biostratigraphic markers are not globally synchronous; their ages could be influenced by factors such as geographic isolation, tectonic obstruction, and climate. Therefore, when the depth and age uncertainties of each datum are considered, our Bayesian chronology remains consistent with the biostratigraphic data.

A subsequent comparison of our Site U1464 chronology with recent chronostratigraphic studies of NWS sediments reveals some inconsistencies. For example, dynamical time warping was employed to align a portion of the Site U1464 wireline natural gamma ray (NGR) record (on depth) to that of neighbouring Site U1463 (Groeneveld et al., 2021). Conversion of the U1464 wireline depths to the CCSF depths using the dynamically warped NGR reveals that all seven biostratigraphic markers (i.e., Top *G. fistulosus*, Base *G. truncatulinoides*, Top *G. extremus*, Top *G. limbata*, Base *G. inflata*, Top *G. exilis* and Top *G. pseudomiocenica*) from Groeneveld et al. (2021) lie outside our 99.99% confidence intervals (green crosses in Figure S7). Some biostratigraphic markers (i.e., Base *G. inflata*, Top *G. exilis* and Top *G. pseudomiocenica*) from Site U1463 had never been documented at Site U1464, and using these markers would violate the principle of biostratigraphy at Site U1464. This result shows that the dynamical time warping

projections from Site U1463 cannot directly be used as new age constraints for Site U1464, as emphasized in Groeneveld et al. (2021). In addition, wireline logs (e.g., NRG) records from upper Pleistocene sediments at Site U1463 and Site U1464 show weak signals (Gallagher et al., 2017a, 2017b; Groeneveld et al., 2021). This may also lead to uncertainties in dynamic warping between Site U1463 and Site U1464, such as observed in Figure S7.

Furthermore, there are some offsets between the shipboard ages of seven biostratigraphic markers (i.e., Top *G. fistulosus*, Base *G. truncatulinoides*, Top *G. extremus*, Top *G. limbata*, Base *G. fistulosus*, Base *G. tosaensis* and Top *D. altispira*) at Site U1464 based on the Geological Time Scale 2012 (Gallagher et al., 2017a) and re-calibrated ages of these markers at Site U1463 based on a revised chronostratigraphy (Groeneveld et al., 2021) (purple crosses on Figure S7). It is difficult to ascertain which biostratigraphic markers are more/less reliable, especially as dating NWS sediments from IODP Expedition 356 has not been straightforward (Gallagher et al., 2017a; Groeneveld et al., 2021). There appears to be diachroneity of some biostratographic datums (Gallagher et al., 2017a; Groeneveld et al., 2021), magnetic intensities (for magnetostratigraphy) are weak (Gallagher et al., 2017a, 2017b), and $\delta^{18}O$ stratigraphy is either absent or presents a noisy signal due to the shallow water depths of the drilled sites (Groeneveld et al., 2021; Pei et al., 2021; Stuut et al., 2014, 2019). While our inferred U1464 ages may be up to 200 kyr older at ~60-90 m and ~130 m, shifting our age-depth relationship in that direction would be at odds with the majority of the biostratigraphic datums, as well as with the eccentricity tuning.

For the eccentricity tuning, we attempted 12 different tunings (Figure S6; Table S4; Supporting Information Text S1), but all alternatives resulted in too much stretching/squeezing (hence unrealistic sedimentation rates and changes) or inconsistent eccentricity-$CaCO_3$ relationships (Figure S6). The age difference between the initial age model based on biostratigraphy and the four tie points based on eccentricity tuning is acceptable on the 400 kyr timescale. Therefore, in light of the compatibility of the Bayesian model with biostratigraphy and orbital tunings, we consider this chronology to be sufficiently robust for Site U1464, bearing in mind the aforementioned caveats.

4. Results and Discussion

4.1. Carbonate variations at IODP Site U1464

The calibrated scanning XRF results show that $CaCO_3$ and Sr have consistent variations (Figure 3), indicative of their marine biogenic origins (Rothwell & Croudace, 2015). Although Rb and Zr are not calibrated, Fe, Ti, Rb and Zr also show similar trends (Figure 3), which indicate terrigenous origins as these are typical detrital elements (Rothwell & Croudace, 2015). As expected from the closed-sum effect, marine and terrigenous variations show an inverse relationship (Figure 3), hence their co-variability could be driven by some combinations of marine carbonate production, carbonate dissolution, or dilution by terrigenous inputs. Calculated MARs cannot confirm whether carbonate production/dissolution or terrigenous dilution predominated on the long-term co-variation, because chronology-imposed sedimentation rates controlled the MARs variations (Figure S8).

However, the component-free calculation shows that the terrigenous-free Sr, as well as $CaCO_3$-free Fe and Ti largely maintained their original trends, indicating that the dilution of each component did not control the observed long-term trends (Figure S8). The Log(Sr/Ca) has successfully been calibrated against XRD-derived aragonite in carbonates on the NWS, based on aragonite being characterized by high Sr (Hallenberger et al., 2019, 2022). As a proxy of aragonite content in total carbonates, the Log(Sr/Ca) is not influenced by terrigenous dilution. The consistently positive correlation between %$CaCO_3$ and Log(Sr/Ca) at Site U1464 indicates that the dominant processes controlling trends are $CaCO_3$ production and dissolution, rather than changes in terrigenous input (Figure S3). Additionally, the clr(Ca) and clr(Sr) are less sensitive to terrigenous dilution, and their long-term consistency with calibrated $CaCO_3$ and Sr further suggests that terrigenous dilution of $CaCO_3$ is minor within our investigated interval at Site U1464 (Figure S3). This inference is consistent with low Al and K concentrations in ICP-OES and scanning-XRF results from Site U1464 during our study interval, indicating a minor clay-bound fine-grained fraction likely transported to the NWS by run-off (Kuhnt et al., 2015; Rothwell & Croudace, 2015; Zhang et al., 2020). Eolian dust may contribute to the dilution of %$CaCO_3$, however a comparison between %$CaCO_3$ and dust records suggests that this dilution effect is not significant over the 400 kyr timescale (Figure 6; Figure 7; see Section 4.2).

Percentage carbonate at Site U1464 was relatively elevated at ~2.89-2.74 Ma, ~2.46-2.34 Ma, ~2.13-1.89 Ma and ~1.71-1.58 Ma. These broad variations are consistent with the %$CaCO_3$ record on an independent benthic $\delta^{18}O$ chronology at IODP Site U1482 (~1465 m water depth at present, Chen et al., 2022) on the northern edge of the NWS (Figure 6a), validating our eccentricity tuning method. The 400 kyr cycliciy in these $CaCO_3$ records differs from Pleistocene deep-sea $CaCO_3$ records, which generally follow a glacial-interglacial pattern thought to be primarily driven by dissolution (Sexton & Barker, 2012). Lack of a glacial-interglacial pattern indicates that shallow $CaCO_3$ burial on the NWS was not responding directly to global sea-level during the early Pleistocene. A similar cyclicity to that seen in $CaCO_3$ variations is also found in benthic $\delta^{13}C$ at IODP Site U1482, and to a lesser degree in benthic $\delta^{13}C$ at nearby Site U1463 (Figure 6b, c), where 400 kyr variability has been identified over the ~5.2-1.7 Ma interval (Groeneveld et al., 2021). We next focus on and interpret the covariation between Site U1464 $CaCO_3$ and Site U1482 $CaCO_3$ and $\delta^{13}C$ records, and suggest that a common process controlled their eccentricity-scale covariations. To investigate the cause of this carbon cycle pacing, we propose two processes (biology and water-mass mixing), and then possible origins of the 400 kyr eccentricity forcing are discussed.

4.1.1. Biological processes

Biological processes that modulate both $CaCO_3$ burial and the $\delta^{13}C$ of benthic foraminiferal tests include primary productivity (amount and which phytoplankton functional groups dominate), $CaCO_3$ production (calcification), as well as water column/seafloor/post-depositional $CaCO_3$ dissolution (itself controlled by carbonate saturation state) and organic matter remineralization.

Calcifying organisms on the NWS mainly consist of coccolithophores, planktonic/benthic foraminifera, pteropods, coralline algae and bryozoans (Gallagher et al., 2017a, 2017b; Hallenberger et al., 2019, 2022; James et al., 2004). $CaCO_3$ production and export from the surface ocean are influenced by changes in the morphology and abundance of coccolithophores and other potentially calcifying plankton. Coccolith $CaCO_3$ export is proposed to have varied over eccentricity ~400 kyr timescales as an evolutionary response to eccentricity forcing on tropical seasonality, with maximum coccolith $CaCO_3$ export and burial in sediments during eccentricity minima (Beaufort et al., 2021). Biological $CaCO_3$ production could explain the pacing between $CaCO_3$ and benthic $\delta^{13}C$ records on the NWS, if high primary productivity

promoted $CaCO_3$ production and enriched seawater $\delta^{13}C$ via photosynthesis. Although abiotic carbonate (aragonite and dolomite) production on the NWS could be driven by climate and sea-level (Gallagher et al., 2018; Hallenberger et al., 2019; 2022; Reuning et al., 2022), the 400 kyr pacing between $CaCO_3$ and benthic $\delta^{13}C$ cannot be attributed to these abiotic processes.

In parallel to changes in $CaCO_3$ production and export, shallow $CaCO_3$ dissolution on the NWS may have occurred in the water column, on the seafloor and in the sediment primarily driven by metabolic release of CO_2, especially localized low-$[CO_3^{2-}]$ due to microbial degradation of organic matter (James et al., 2005; Reuning et al., 2022; Schulte & Bard, 2003; Sulpis et al., 2021; Ziveri et al., 2023). The relationship between carbonate dissolution and organic matter degradation has been demonstrated in previous studies, where they showed that aragonite or/and calcite dissolution was strongly in phase with orbital controlled productivity and associated degradation of organic matter (Reuning et al., 2022; Schulte & Bard, 2003). This organic matter degradation-driven $CaCO_3$ dissolution might, in part, explain the consistency between $CaCO_3$ and benthic $\delta^{13}C$ records on the NWS. With the available data, it remains uncertain whether carbonate production or dissolution was the more important control on $CaCO_3$ burial at Site U1464, however biological processes appear to have played an important role in carbon cycle pacing on the NWS.

4.1.2. Water-masses mixing processes

The seafloor at Site U1464 is currently bathed by the Leeuwin Undercurrent (LUC), and its water masses mainly derive from Sub-Antarctic Mode Water (SAMW) and/or Antarctic Intermediate Water (AAIW) via the Flinders Current offshore South Australia (Herraiz-Borreguero & Rintoul, 2011; Richardson et al., 2019; Wijeratne et al., 2018; Wong, 2005; Woo & Pattiaratchi, 2008). The corrosivity (degree of carbonate saturation) of SAMW and AAIW would intensify as the water flows further from its sources, accumulating more depleted $[CO_3^{2-}]$ and $\delta^{13}C$ from the respiration of organic matter. Observational data show that modern SAMW and AAIW are injected northward into the Indian Ocean at ~15°S (Figures S9, S10; Herraiz-Borreguero & Rintoul, 2011; Ridgway & Godfrey, 2015; Wong, 2005), and this northward penetration extends to Site U1464.

P. wuellerstorfi $\delta^{13}C$ at Deep Sea Drilling Project (DSDP) Site 593 mainly reflects the dissolved inorganic carbon $\delta^{13}C$ of intermediate water, which is primarily southern-sourced

AAIW with minor local contributions (Elmore et al., 2015; McClymont et al., 2016). *P. wuellerstorfi* $\delta^{13}C$ at Site U1482 records the dissolved $\delta^{13}C$ of Indonesian Intermediate Water (IIW), which originates from AAIW in the western Pacific (Figure S9b, c; Figure S10b, c) (Talley & Sprintall, 2005; Zenk et al., 2005; Wong, 2005). Thus, the intrusion intensity of AAIW to Sites U1464 and Site 593, and indirectly to Site U1482, or/and changes in AAIW $[CO_3^{2-}]$ and $\delta^{13}C$ due to ventilation variations, may explain co-variability in the respective $CaCO_3$ and $\delta^{13}C$ records (Figure 6). In addition, the proximity of Sites U1464 and U1482 suggests a more direct influence of regional water masses. At Site U1482, dissolved $[CO_3^{2-}]$ is high in surface waters due to photosynthesis and decreases with depth as organic matter degrades (Figure S9a, S10a). Dissolved $\delta^{13}C$ in the water column may also reflect this biological process, whereby surface/intermediate waters are characterized by heavier/lighter $\delta^{13}C$, respectively. Indonesian surface waters feed the south-flowing Leeuwin Current which overlies the Australian NWS; hence, the ventilation and mixing of intermediate and surface waters at Sites U1482 and U1464 could account for close covariation in their respective $\delta^{13}C$ and $CaCO_3$ records (Figure 6).

4.1.3. Origin of the 400 kyr eccentricity forcing

A pervasive ~400 kyr signature has been observed widely in Cenozoic and Mesozoic $CaCO_3$ and foraminiferal $\delta^{13}C$ records (Beaufort et al., 2021; Herbert et al., 1997; Holbourn et al., 2007; Kochhann et al., 2016; Kocken et al., 2019; Liebrand et al., 2016; Moore et al., 1982; Pälike et al., 2006; Rickaby et al., 2007; Wang et al., 2010; Westerhold et al., 2011; Woodruff & Savin, 1991), indicating a response of the ocean carbon reservoir to 400 kyr eccentricity. The 400 kyr eccentricity minima could correspond to periods of enhanced carbonate production in some parts of the ocean (Beaufort et al., 2021; Liebrand et al., 2016; Rickaby et al., 2007), decreased carbonate dissolution and positive $\delta^{13}C$ shifts in others (Holbourn et al., 2007; Kochhann et al., 2016; Westerhold et al., 2011; Woodruff & Savin, 1991). A full understanding of ~400 kyr ocean carbon cycles is beyond the scope of this study, however we briefly describe three possible hypotheses (tropical seasonality, chemical weathering and organic carbon sequestration) to account for the linkage between ~400 kyr eccentricity cycles and $CaCO_3$ at Site U1464.

Previous studies suggested that Earth's orbital eccentricity modulated the evolution, morphology and carbonate production of calcifying phytoplankton (e.g., coccolithophores) throughout the Pleistocene (Beaufort et al., 2021; Rickaby et al., 2007). Reduced seasonality during eccentricity minima in surface ocean conditions could favour the dominance of opportunistic calcifying species with high carbonate export and burial and *vice versa* (Beaufort 2021). Chemical weathering has been proposed as a potential driver of the ~400 kyr ocean carbon cycle via carbon/nutrient inputs (Ma et al., 2011). In this hypothesis, a decrease in carbon/nutrient input during eccentricity minima due to decelerated chemical weathering can reduce marine primary productivity, which can lead to maxima of bottom-water $\delta^{13}C$ and improved $CaCO_3$ preservation in response to decreased respired CO_2 release at the seafloor and in the sediments. Organic carbon sequestration may be an alternative mechanism forced by eccentricity (DeConto et al., 2012; Kocken et al., 2019; Zeebe et al., 2017). Year-round relatively wet and cold conditions during eccentricity minima would promote anoxia and organic carbon sequestration in terrestrial soils (Zeebe et al., 2017), terrestrial permafrost (DeConto et al., 2012) and marine sediments (Kocken et al., 2019), resulting in a ^{13}C- and $[CO_3^{2-}]$-enriched ocean carbon pool.

In contrast to Plio-Pleistocene climate proxy records (e.g., ice volume and monsoon) (Grant et al., 2022; Lisiecki & Raymo, 2005; Stuut et al., 2019), precession and obliquity periodicities are both absent from the ~1 kyr resolution $CaCO_3$ record at Site U1464. The amplification of ~400 kyr cycles in our $CaCO_3$ record could be caused by power transfer processes from high to low frequencies, such as the long residence time of carbon in the oceans (~100 kyr) and nonlinear responses to forcing values (Herbert et al., 1997; Pälike et al., 2006; Zeebe et al., 2017). Additionally, post-depositional processes may have smoothed out precession and obliquity signals in the $CaCO_3$ record. For example, partial carbonate dissolution and reprecipitation could have distorted the higher frequency cycles, as observed in the formation of diagenetic carbonates and 'frosty' foraminifera at Site U1464 (Zhao et al., 2024).

4.2. Eolian input to IODP Site U1464

Log(Zr/Fe) has been used at ODP Site 762 (Figure 1) as a proxy for eolian dust from Northwest Australia (Stuut et al., 2014, 2019). Log(Zr/Fe) can indicate the transport pathway and grain-size of terrigenous particles since the wind-blown fraction is enriched in Zr due to its presence

in coarser and/or heavier grains, whereas Fe is enriched in run-off sediments (Stuut et al., 2014, 2019). We also use Log(Zr/Rb) as a dust proxy, as Rb is preferentially incorporated into riverine fine-grained clays (Pei et al., 2021; Rothwell & Croudace, 2015). The Log(Zr/riverine element) ratio is therefore used to estimate the relative contribution of eolian versus riverine inputs.

Isothermal remanence magnetism (IRM) has also been used to approximate past eolian dust flux in marine cores (Larrasoaña et al., 2003; Grant et al., 2022), where the IRM remaining after AF demagnetization at 170 mT ($IRM_{1T@AF\ 170mT}$) reflects the relative contribution from magnetic minerals with a coercivity of remanence larger than 170 mT (i.e., imperfect antiferromagnetic minerals, such as hematite) (Verosub & Roberts, 1995). Hematite is generally thought to be preferentially formed in dry and hot environments and then transported to marine sediments via eolian dust. The long-term consistency of magnetic susceptibility, ARM, IRM_{1000mT}, $IRM_{1T@AF170mT}$ with $CaCO_3$-free $IRM_{1T@AF\ 170mT}$ indicates that their variations represent the changes in magnetic mineral concentrations and that these are not driven by carbonate dilution, despite some differences in short-term variations (Figure S11). However, it is not straightforward to use the magnetic susceptibility, ARM, IRM_{1000mT} as eolian dust proxies. Thus, we do not use these magnetic parameters herein. The results of uncertainty propagation demonstrate broadly consistent long-term trends and high-frequency co-variability in the obliquity band between our magnetic hematite proxy and geochemical dust proxies (Figure 7a-c, Figure S12, note reversed y-axes; see Supporting Information Text S2), corroborating their interpretation as eolian dust proxies at Site U1464.

For comparison, a Log(Zr/Fe) record is available for ODP Site 762 offshore Northwest Australia (Stuut et al., 2019) (Figure 1; Figures 7e). In terms of absolute values, Log(Zr/Fe) at Site U1464 has higher values than that at ODP Site 762 during the same period. Discrete samples from modern river beds and dune sediments in Northwest Australia showed that Log(Zr/Fe) values of dune sediments are generally greater than -1, while those in river beds are typically less than -1 (Stuut et al., 2019). If modern end-member values are applicable over the late Pliocene/early Pleistocene, it implies that Site U1464 Log(Zr/Fe) values mostly reflect dune end-members (based on a 21-point running average (Figure 7c), although some individual data points are less than -1), while ODP Site 762 Log(Zr/Fe) values reflect riverine sources (Figure 7e). At first glance, this observation appears counter-intuitive, as Site 762 is located further offshore than Site

U1464 (Figure S1) and, the proportion of riverine (eolian) components in off-shore sediment tends to decrease (increase) with distance from river mouths (Stuut et al., 2019). However, ODP Site 762 is more proximal to outflow from the Fortescue, Ashburton and Lyndon-Minilya rivers than Site U1464 (Figure S1), which, in contrast, lies directly in the path of the Northwest Australian dust belt (Figure S1, Bowler, 1976). An additional/alternative explanation is that Site U1464 lies on the shelf slope at ~260 m water depth, while ODP Site 762 is further offshore at 1360 m water depth, so prevailing currents and sediment dynamics/transport differ between the sites. Inconsistent trends between Site U1464 and Site 762 Log(Zr/Fe) records may, therefore, be explained by their contrasting locations and associated differences in the proportion of riverine/dust components reaching each site. Chronological offsets/uncertainties could also explain some discrepancies between the records, although it is hard to explain such differing trends by chronology alone (e.g., the records are almost anti-phased between ~2.9 and ~2.4 Ma).

Better agreement is observed between our IODP Site U1464 Log(Zr/Fe) record and a downhole natural gamma radiation (NGR)-derived Th/K record from neighboring IODP Site U1463 (Christensen et al., 2017) (Figure 1; Figure 7d), taking into account the chronological uncertainties/offsets between these sites. The Th/K – a proxy of weathering in the hinterland – record has been interpreted to represent dust accumulation at Site U1463 (Christensen et al., 2017). Potentially synchronous maxima between the U1463 Th/K and our U1464 dust proxy records can be identified (dashed lines in Figure 7a-d). Nonetheless, there are also uncertainties in NGR-derived K and Th measurements (De Vleeschouwer et al., 2017), which would account for some of the observed discrepencies between our U1464 dust proxy records and the Site U1463 Th/K record. One limitation is that the wireline NGR system integrates counts from a 20-cm region surrounding a core, which causes significant smoothing of signals during measurements. Also, the algorithm that produces estimates of K and Th content relies on different density measurements (gamma ray attenuation, moisture and density), and these density measurements can contribute additional errors to the K and Th estimates.

4.3. Obliquity-paced Northwest Australian dust flux

Spectral analyses of our dust records reveal significant peaks corresponding to three obliquity frequencies (at ~0.024 kyr^{-1} (41 kyr), ~0.034 kyr^{-1} (29 kyr) and ~0.019 kyr^{-1} (54 kyr), following Hinnov (2000) and Mélice et al. (2001)) using the Redfit method (Figure S5c-e). These three

frequencies are also observed in the Multitaper method (Figure S5h-j). Furthermore, the position and relative amplitude of the 0.019 kyr^{-1} peak, and to a lesser extent, the 0.034 kyr^{-1} peak, are relatively insensitive to our obliquity tuning and Bacon age modelling (Figure S5; Figure S13), underscoring the reliability of our spectral analyses and the dominance of obliquity in Site U1464 dust-flux proxy records. Spectral power in the precession band is less pronounced and limited to ~0.051 kyr^{-1} (Figure S5). Interestingly, the 0.019 and/or 0.034 kyr^{-1} frequencies have also been detected in Australian monsoon records (Holbourn et al., 2005; Kershaw et al., 2003; Liu et al., 2015; Zhang et al., 2020, 2022) and in eolian grain size records from other Indo-Pacific regions (Clemens & Prell, 1990; Hovan et al., 1991; Pisias & Rea, 1988), suggesting that these frequencies may be a consistent feature of large-scale atmospheric circulations through the Plio-Pleistocene (see Section 4.4 below).

The spectral peak in Site U1464 dust proxies at ~41 kyr could be explained by a linear response to obliquity forcing, since this is the dominant period of obliquity. However, the amplitude of the ~54 kyr peak in our dust proxies is much higher than that of the 41 kyr peak, contrary to the obliquity spectrum (Hinnov, 2000; Laskar et al., 2004; Mélice et al., 2001); the 54 kyr peak may therefore reflect a non-linear response to obliquity forcing or a heterodyne of other orbital frequencies. To investigate the evolution of these two obliquity periods in our time-series, we calculated bandpass-filters of 0.023-0.027 kyr^{-1} and 0.017-0.021 kyr^{-1} in Log(Zr/Rb), and found that the amplitude of varibility at the 0.024 kyr^{-1} frequency was higher during the ~2.9-2.24 Ma interval, while the amplitude of varibility at the 0.019 kyr^{-1} frequency was higher after ~2.1 Ma (Figure S14b, c). This frequency shift from 0.024 to 0.019 kyr^{-1} might be attributed to ~1.2-Ma obliquity amplitude modulation (AM), which decreased during the interval of 2.24-2.1 Ma (Figure S14a) (Hinnov, 2000; Laskar et al., 2004). The transformation from AM into frequency modulation (FM) seems consistent with previously proposed FM hypotheses, in which a high-frequency carrier can be modulated by a low-frequency modulator to create sidebands based on $F_{Carrier} \pm F_{Modulator} = F_{Sideband}$ (Rial, 1999; Rial & Anaclerio, 2000). In this case, the 0.019 (1/54) kyr^{-1} peak in our observation coincides with the sideband of a 0.024 (1/41) kyr^{-1} carrier modulated by a 0.005 (1/171) kyr^{-1} modulator; that is 0.024 - 0.005 = 0.019, in which the ~0.005 (1/171) kyr^{-1} originates from the obliquity AM (Hinnov, 2000; Mélice et al., 2001). Similarly, the 0.034 (1/29) kyr^{-1} peak may also be the sideband of a 0.024 (1/41) kyr^{-1} modulated by the

0.005 (1/171) kyr^{-1} (i.e., 0.024 + 2*0.005 = 0.034). The specific origins of these obliquity signals will be further discussed in the following section.

4.4. Origin of obliquity signals in Northwest Australian dust records

Here, we explore possible origins of the dominant obliquity-scale variability in our dust proxy records and what this reveals about the forcing of Australian dust flux over orbital timescales. Two key forcings to consider are i) high-latitude forcing via eustatic sea level and/or the East Asian winter monsoon (EAWM) and ii) direct low-latitude insolation forcing via the summer inter-tropical insolation gradient (SITIG). Both of these mechanisms show strong obliquity periodicities and have been proposed to explain the presence of obliquity cycles in low-latitude monsoon and eolian dust flux records (Beck et al., 2018; Ding et al., 2002; Hennekam et al., 2022; Leuschner & Sirocko, 2003; Liu et al., 2015; Stuut et al., 2019; Sun et al., 2006).

4.4.1. High-latitude forcing: eustatic sea level and the EAWM

Glacial cycles may influence the NWS dust flux through eustatic sea level and/or the EAWM. Sea-level fluctuations alter the distance between the coastline and Site U1464, affecting the dilution of dust by fluvial sediments, with increased fluvial dilution occurring during glacial lowstands (Stuut et al., 2019). Moreover, the extent of northern hemisphere ice sheets determines the temperature gradients from pole to equator, which in turn influence the position and strength of atmospheric circulations (e.g., EAWM) and, consequently, global climate (Clark et al., 1999; Ganopolski et al., 1998). For example, the ice-sheet fluctuations could modulate EAWM intensity on obliquity timescale, which was directly coupled to the Australian monsoon via cross-equatorial flows (Ding et al., 2002; Liu et al., 2015; Sun et al., 2006; Suppiah, 1992; Suppiah & Wu, 1998). To further investigate the relative importance of sea level forcing versus EAWM forcing, we compare our dust records to a global sea level reconstruction (Rohling et al., 2021) and to a stacked mean grain-size of quartz (MGSQ) record from the Chinese Loess Plateau, which represents EAWM strength (Sun et al., 2006) (Figure 8a-d).

This comparison revealed that our Australian dust-flux reconstructions do not show consistent phasing with sea level, despite both exhibiting high power in the 41 kyr obliquity band (Figure 8a, b; Figure S13a). This suggests that the 41 kyr cycles in our dust proxies were unlikely influenced by fluvial dilution resulting from eustatic sea-level fluctuations. This conclusion aligns with our geochemical records, which indicate that the terrestrial sediments at Site U1464

are predominantly composed of eolian dust, with an estimated paleodepth exceeding 300 meters during the early Pleistocene (Gallagher et al., 2017a), and the absence of significant riverine sources at this site (Figure S1). From these observations, we can rule out eustatic sea level as a forcing mechanism, consistent with previous studies on the Pleistocene South Asian summer monsoon based on Arabian Sea sediments (Clemens et al., 1991a; Clemens & Prell, 2003; Leuschner & Sirocko, 2003) and the early Pleistocene North African monsoon based on eastern Mediterranean Sea sediments (Hennekam et al., 2022; Reichart, 1997). We suggest that, rather than via eustatic sea level forcing, ice sheet fluctuations may have imparted 41 kyr variability on the NWS dust records via the EAWM.

Comparison between Site U1464 Log(Zr/Fe) and the stacked MGSQ record reveals that Northwest Australian dust flux had a similar, but anti-phased, long-term relationship to EAWM intensity (Figure 8c). In general, decreased dust flux off Northwest Australia corresponds to a stronger EAWM, and *vice versa*. A straightforward explanation is that enhanced EAWM intensity would favor a stronger Australian summer monsoon, expanded vegetation cover, less erodible particles in source areas, and dampening of southeast trade winds which transport dust from the Australian interior towards the NWS. Three peaks associated with obliquity frequencies are present in both records over the 1.6-2.9 Ma interval (Figure S13b, d-f); however, cross-wavelet analysis suggests an ambiguous relationship between Site U1464 dust flux and EAWM variability at obliquity frequencies (Figure 8d). This inconsistency may be an artifact that different obliquity phasings were assumed in the orbital tuning of the two records. The stacked MGSQ chronology involves an assumed 8-kyr lag with respect to obliquity (Ding et al., 2002; Sun et al., 2006), while we assumed zero phase lag between Site U1464 dust flux and obliquity in this study. Additionally, we applied an age uncertainty of ±20-kyr for the obliquity tuning tie-points in our Bacon age model. The 8-kyr lag for the MGSQ record is based on SPECMAP (Imbrie et al., 1984); hence, it is based on relatively large amplitude glacial-interglacial cycles of the late Pleistocene, whereas a smaller lag should be expected for the early Pleistocene. Equally, there may be an ice-volume effect on our dust records, via the EAWM, in which case a lagged obliquity tuning may be more appropriate. Therefore, although we cannot objectively compare the obliquity-band phasing of our dust records with the stacked MGSQ record, we nonetheless propose EAWM intensity as a possible, but antiphased, origin of the obliquity cycles observed in our Site U1464 dust-flux time series, given the similarity of their long-term trends and obliquity-

band spectral peaks, and a known physical mechanism (cross-equatorial flow) linking the two monsoon regions.

4.4.2. Low-latitude SITIG forcing

The SITIG (i.e., the difference in summer insolation between 30 ^{o} N and 30 ^{o} S) is a low-latitude insolation forcing which contains notable precession and obliquity components (unlike 30 ^{o} N and 30 ^{o} S insolation time-series), and has been invoked as a potential driver of East Asian (Beck et al., 2018), Indian (Leuschner & Sirocko, 2003) and African monsoon (Reichart, 1997) variability over orbital timescales. This forcing mechanism has been corroborated by model simulations and has a physical basis as described by previous studies (Beck et al., 2018; Bosmans et al., 2015; Mantsis et al., 2014). In this mechanism, a stronger SITIG can drive an intensified winter Hadley circulation and thus a stronger cross-equatorial moisture transport into the summer hemisphere, and this has been shown on seasonal (Schwendike et al., 2014) and orbital timescales (Beck et al., 2018; Bosmans et al., 2015; Mantsis et al., 2014).

Obliquity plays a key role in modulating the SITIG and meridional heating gradients. Several modelling studies have demonstrated that when the SITIG is stronger during higher obliquity, high-pressure anticyclones in the Southern Hemisphere (which form the descending limb of the winter hemisphere Hadley cell) are strengthened, while high-pressure anticyclones in the Northern Hemisphere (which form the descending limb of the summer hemisphere Hadley cell) are weakened (Beck et al., 2018; Bosmans et al., 2015; Mantsis et al., 2014; Schwendike et al., 2014). Thus, during a stronger obliquity-induced SITIG, intensified cross-equatorial winds and moisture transport into the Northern Hemisphere is consistent with intensified southeasterly trade winds and a more arid Australian interior, and *vice versa*. Northwest Australian dust flux can therefore respond immediately to changes in the SITIG via these dynamics. Since muted precession and large obliquity are present in Site U1464 dust proxy records (Figure S5), the summer half-year (21 March - 20 September), instead of one single month, was calculated in the SITIG as follows: SITIG = $I_{March\text{-}September}$ (30 ^{o} N) - $I_{March\text{-}September}$ (30 ^{o} S), where $I_{March\text{-}September}$ (30 ^{o} N or 30 ^{o} S) is sum of monthly insolation from 21 March to 20 September at 30 ^{o} N or 30 ^{o} S. This calculation can amplify obliquity and mute precession (Figure S13c), and is hence more consistent with our observations. There is reasonable agreement between Site U1464 dust flux and SITIG before 2.55 Ma and after 2.35 Ma (Figure 8e, f) in both frequency and amplitude

variability. Between 2.55 and 2.35 Ma, the records appear to be offset, i.e., there appears to be a phase lag of dust flux relative to the SITIG. Given that we assumed no phase lag in our obliquity tuning (based on the near-direct mapping of the filtered Log(Zr/Rb) onto obliquity prior to tuning, Figure 5), comparison of the SITIG to our dust proxy record cannot include interpretation of phase relationships. Nonetheless, the agreement through most of the records in both amplitude and dominant frequency is consistent with SITIG forcing of Northwest Australian dust flux through the early Pleistocene.

An additional consideration is that the 54 kyr obliquity cycle in our dust records might be amplified by a nonlinear response to the AM of obliquity (and hence to the resultant SITIG). For example, the long-term mean of the SITIG AM narrowed down to a lower value during ~2.24-2.1 Ma due to the 1.2-Myr obliquity AM (Figure S14a), and the decreased amplitude of SITIG variability, amplified by internal climate feedbacks, could have shifted the sensitivity of Northwest Australian dust flux to SITIG forcing from a 41 kyr cycle to a prolonged 54 kyr cycle (Figure S14b, c). On the one hand, a smaller amplitude in the SITIG would reduce the relative strength of winter Hadley circulation and associated cross-equatorial flows between SITIG maxima and minima, thereby weakening the 41 kyr effect on dust flux over Northwest Australia. On the other hand, smaller SITIG amplitude after ~2.1 Ma would make the 171 kyr AM cycle comparable or stand out relative to the 41 kyr cycle, which would explain the presence of 171 kyr cycles in our dust records (Figure S14a, d, e). The 54 kyr spectral peak is dominant over the 41 kyr peak in our dust records, especially after ~2.1 Ma (Figure S14b, c, d, e), and may have been amplified by a FM mechanism based on 0.024 (1/41) - 0.005 (1/171) = 0.019 (1/54) (Rial, 1999; Rial & Anaclerio, 2000).

4.4.3. Insights from other Indo-Pacific dust records

Orbitally-driven changes in the intensity of the EAWM, the SITIG, or both, may underpin the dominant obliquity cycles observed in Site U1464 dust-flux reconstructions. For further insights, we therefore turn to other Indo-Pacific dust records. Interestingly, dust-flux time-series from Site RC27-61 in the northwestern Arabian Sea (Clemens & Prell, 1990; Clemens et al., 1991a), Site RC11-210 in the central Equatorial Pacific (Pisias & Rea, 1988) and Site V21-146 in the Northwest Pacific (Hovan et al., 1991) all contain cycles at 54 and/or 29 kyr, in addition to 41 kyr, similar to our Site U1464 dust records. Australian monsoon records also show these three

obliquity cycles (Holbourn et al., 2005; Kershaw et al., 2003; Liu et al., 2015; Zhang et al., 2020, 2022), while these spectral peaks are not present in the sea level time-series spanning this timeframe (Figure S13a). These findings imply that our Site U1464 dust-flux reconstruction likely reflects a component of low-latitude, Indo-Pacific climate variability that is independent of sea-level related variability.

The long-term variability of Walker circulation and sea surface temperature (SST) gradients in the tropical Pacific and Indian Ocean (i.e., ENSO-like) might amplify the 29 kyr cycles via resonance with obliquity (Beaufort et al., 2001; Pisias & Rea, 1988). The 29 kyr period was dominant in easterly trade wind intensity and equatorial divergence in the central Equatorial Pacific during the late Pleistocene, based on eolian grain-size and relative abundance of two radiolarian species, respectively (Pisias & Rea, 1988). This 29 kyr cycle was also found as a secondary period in: central Equatorial Pacific SST (Pisias & Rea, 1988); southern subtropical Indian Ocean SST (Clemens et al., 1991a, b); wind strength of the southwest monsoon in the northwestern Arabian Sea (Clemens & Prell, 1990; Clemens et al., 1991a, b); and primary productivity associated with the tropical Indo-Pacific thermocline (Beaufort et al., 2001). This non-primary 29 kyr variability inherent in these records suggests that the resonance between obliquity and tropical Indo-Pacific atmosphere-ocean dynamics may play a key role in amplifying the 29 kyr variability in our dust records.

5. Conclusions

This study presents %$CaCO_3$ and eolian dust proxy records (Log(Zr/Rb), Log(Zr/Fe) and $CaCO_3$-free $IRM_{1T@AF\ 170mT}$) for IODP Site U1464 on the Australian Northwest Shelf spanning the early Pleistocene (~1.6 - 2.9 Ma). We introduce a novel, orbitally-tuned chronology developed through a Bayesian model that integrates biostratigraphic datums with eccentricity and obliquity tuning of our %$CaCO_3$ and Log(Zr/Rb) time series.

A ~400 kyr (eccentricity) cyclicity is present in the %$CaCO_3$ record. This is similar to $CaCO_3$ and benthic $\delta^{13}C$ records from the wider region, where the benthic records are typically indicative of intermediate water $\delta^{13}C$, and where $CaCO_3$ and $\delta^{13}C$ maxima are associated with minima in the 400 kyr eccentricity cycle (and *vice versa*). These observations are consistent with a ~400 kyr pacing of the oceanic carbon reservoir via biological and water-masses mixing processes.

Obliquity frequencies dominate the dust proxy records at Site U1464. Three obliquity cycles (41 kyr, 54 kyr and 29 kyr) are present and we explore their possible origins in terms of low- *versus* high-latitude forcing mechanisms. The 41 kyr signal in Northwest Australian dust flux may originate from fluctuations in the intensity of the EAWM and/or the SITIG, both of which are directly driven by obliquity variations. In contrast, the 54 kyr signal in the dust-flux records might result from a non-linear response to AM of obliquity and attendant SITIG variability. The resonance between obliquity and tropical Indo-Pacific atmosphere-ocean dynamics may also be an amplifying mechanism of secondary obliquity frequencies, especially for the 29 kyr cycle, which has been detected in other paleoclimate proxy records from the Indo-Pacific region.

Acknowledgments

This work used samples and data provided by the the International Ocean Discovery Program (IODP) and was supported by the Australian Research Council (ARC) through grant DE1900100042 (K.M.G), the Australia-New Zealand IODP Consortium (ANZIC) Legacy/Special Analytical Funding grant LE160100067 (K.M.G.), the Australian National University-China Scholarship Council (ANU-CSC) Scholarship (S.Z.) and the Shen-su Sun Scholarship (S.Z.). S.G. and G.A. thank the USIO staff and the SIEM Offshore crew for their invaluable assistance and skill during IODP Expedition 356. S.G. thanks the Australian IODP office for funding. We thank Andrew P. Roberts and Xiang Zhao for assistance with measurement and analysis of the environmental magnetic data.

Open Research

Geochemical and environmental magnetic data from IODP Site U1464 were generated in this study. New data are archived in the Zenodo database (Zhao & Grant, 2024).

References

Auer, G., De Vleeschouwer, D., & Christensen, B. A. (2020). Toward a robust Plio-Pleistocene chronostratigraphy for ODP Site 762. *Geophysical Research Letters*, 47(3), e2019GL085198. https://doi.org/10.1029/2019GL085198

Australia's River Basins (1997). Geoscience Australia, Canberra. https://ecat.ga.gov.au/geonetwork/srv/eng/catalog.search#/metadata/42343

Backman, J., Raffi, I., Rio, D., Fornaciari, E., & Pälike, H. (2012). Biozonation and biochronology of Miocene through Pleistocene calcareous nannofossils from low and middle latitudes. *Newsletters on Stratigraphy*, 45(3), 221-244. https://doi.org/10.1127/0078-0421/2012/0022

Baddock, M., Parsons, K., Strong, C., Leys, J., & McTainsh, G. (2015). Drivers of Australian dust: A case study of frontal winds and dust dynamics in the lower Lake Eyre Basin. *Earth Surface Processes and Landforms*, 40(14), 1982-1988. https://doi.org/10.1002/esp.3773

Bailey, I., Hole, G. M., Foster, G. L., Wilson, P. A., Storey, C. D., Trueman, C. N., & Raymo, M. E. (2013). An alternative suggestion for the Pliocene onset of major northern hemisphere glaciation based on the geochemical provenance of North Atlantic Ocean ice-rafted debris. *Quaternary Science Reviews*, 75, 181-194. https://doi.org/10.1016/j.quascirev.2013.06.004

Bayon, G., De Deckker, P., Magee, J. W., Germain, Y., Bermell, S., Tachikawa, K., & Norman, M. D. (2017). Extensive wet episodes in Late Glacial Australia resulting from high-latitude forcings. *Scientific Reports*, 7(1), 1-7. https://doi.org/10.1038/srep44054

Beaufort, L., de Garidel-Thoron, T., Mix, A. C., & Pisias, N. G. (2001). ENSO-like forcing on oceanic primary production during the late Pleistocene. *Science*, 293(5539), 2440-2444. https://doi.org/10.1126/science.293.5539.2440

Beaufort, L., Bolton, C.T., Sarr, A., Suchéras-Marx, B., Rosenthal, Y., Donnadieu, Y., et al. (2021). Cyclic evolution of phytoplankton forced by changes in tropical seasonality. *Nature*, 601, 79 - 84. https://doi.org/10.1038/s41586-021-04195-7

Blaauw, M., & Christen, J. A. (2011). Flexible paleoclimate age-depth models using an autoregressive gamma process. *Bayesian Analysis*, 6(3), 457-474. https://doi.org/10.1214/11-BA618

Beck, J. W., Zhou, W., Li, C., Wu, Z., White, L., Xian, F., et al. (2018). A 550,000-year record of East Asian monsoon rainfall from ^{10}Be in loess. *Science*, 360(6391), 877-881. https://doi.org/10.1126/science.aam5825

Bosmans, J. H. C., Hilgen, F. J., Tuenter, E., & Lourens, L. J. (2015). Obliquity forcing of low-latitude climate. *Climate of the Past*, 11(10), 1335-1346. https://doi.org/10.5194/cp-11-1335-2015

Bowler, J. M. (1976). Aridity in Australia: age, origins and expression in aeolian landforms and sediments. *Earth-Science Reviews*, 12(2-3), 279-310. https://doi.org/10.1016/0012-8252(76)90008-8

Brierley, C. M., & Fedorov, A. V. (2010). Relative importance of meridional and zonal sea surface temperature gradients for the onset of the ice ages and Pliocene-Pleistocene climate evolution. *Paleoceanography*, 25, PA2214. https://doi.org/10.1029/2009PA001809

Chappell, J., Syktus, J., Giambelluca, T. W., & Henderson-Sellers, A. (1996). Palaeoclimatic modelling: A western Pacific perspective. In T. W. Giambelluca and A. Henderson-Sellers (Eds.), *Climate Change: Developing Southern Hemisphere Perspectives* (pp. 175-193). John Wiley & Sons.

Chen, Y., Xu, J., Liu, J., Li, T., Xiong, Z., Zhang, P., & Yan, H. (2022). Climatic and tectonic constraints on the Plio–Pleistocene evolution of the Indonesian Throughflow intermediate water recorded by benthic $\delta^{18}O$ from IODP site U1482. *Quaternary Science Reviews*, 295, 107666. https://doi.org/10.1016/j.quascirev.2022.107666

Christensen, B. A., Renema, W., Henderiks, J., De Vleeschouwer, D., Groeneveld, J., Castañeda, I. S., et al. (2017). Indonesian Throughflow drove Australian climate from humid Pliocene to arid Pleistocene. *Geophysical Research Letters*, 44(13), 6914-6925. https://doi.org/10.1002/2017GL072977

Clark, P. U., Alley, R. B., & Pollard, D. (1999). Northern Hemisphere ice-sheet influences on global climate change. *Science*, 286(5442), 1104-1111. https://www.science.org/doi/10.1126/science.286.5442.1104

Clemens, S. C., & Prell, W. L. (1990). Late Pleistocene variability of Arabian Sea summer monsoon winds and continental aridity: Eolian records from the lithogenic component of deep-sea sediments. *Paleoceanography*, 5(2), 109-145. https://doi.org/10.1029/PA005i002p00109

Clemens, S., Prell, W., Murray, D., Shimmield, G., & Weedon, G. (1991a). Forcing mechanisms of the Indian Ocean monsoon. *Nature*, 353(6346), 720-725. https://doi.org/10.1038/353720a0

Clemens, S. C., & Prell, W. L. (1991b). Late Quaternary forcing of Indian Ocean summer-monsoon winds: A comparison of Fourier model and general circulation model results. *Journal of Geophysical Research: Atmospheres*, 96(D12), 22683-22700. https://doi.org/10.1029/91JD02205

Clemens, S. C., & Prell, W. L. (2003). A 350,000 year summer-monsoon multi-proxy stack from the Owen Ridge, Northern Arabian Sea. *Marine Geology*, 201(1-3), 35-51. https://doi.org/10.1016/S0025-3227(03)00207-X

Courtillat, M., Hallenberger, M., Bassetti, M. A., Aubert, D., Jeandel, C., Reuning, L., et al. (2020). New record of dust input and provenance during glacial periods in Western Australia Shelf (IODP expedition 356, Site U1461) from the Middle to Late Pleistocene. *Atmosphere*, 11(11), 1251. https://doi.org/10.3390/atmos11111251

DeConto, R.M., Galeotti, S., Pagani, M., Tracy, D., Schaefer, K.M., Zhang, T., Pollard, D.D., & Beerling, D.J. (2012). Past extreme warming events linked to massive carbon release from thawing permafrost. *Nature*, 484, 87-91. https://doi.org/10.1038/nature10929

Denniston, R. F., Asmerom, Y., Polyak, V. J., Wanamaker Jr, A. D., Ummenhofer, C. C., Humphreys, W. F., et al. (2017). Decoupling of monsoon activity across the northern and southern Indo-Pacific during the Late Glacial. *Quaternary Science Reviews*, 176, 101-105. https://doi.org/10.1016/j.quascirev.2017.09.014

De Vleeschouwer, D., Dunlea, A. G., Auer, G., Anderson, C. H., Brumsack, H., de Loach, A., et al. (2017). Quantifying K, U, and T h contents of marine sediments using shipboard natural gamma radiation spectra measured on DV JOIDES Resolution. *Geochemistry, Geophysics, Geosystems*, 18(3), 1053-1064. https://doi.org/10.1002/2016GC006715

De Vleeschouwer, D., Auer, G., Smith, R., Bogus, K., Christensen, B., Groeneveld, J., et al. (2018). The amplifying effect of Indonesian Throughflow heat transport on Late Pliocene Southern Hemisphere climate cooling. *Earth and Planetary Science Letters*, 500, 15-27. https://doi.org/10.1016/j.epsl.2018.07.035

Ding, Z. L., Derbyshire, E., Yang, S. L., Yu, Z. W., Xiong, S. F., & Liu, T. S. (2002). Stacked 2.6-Ma grain size record from the Chinese loess based on five sections and correlation with the deep-sea $\delta^{18}O$ record. *Paleoceanography*, 17(3), 5-1. https://doi.org/10.1029/2001PA000725

Ekström, M., McTainsh, G. H., & Chappell, A. (2004). Australian dust storms: temporal trends and relationships with synoptic pressure distributions (1960–99). *International Journal of Climatology: A Journal of the Royal Meteorological Society*, 24(12), 1581-1599. https://doi.org/10.1002/joc.1072

Elmore, A. C. , Mcclymont, E. L. , Elderfield, H. , Kender, S. , Cook, M. R. , & Leng, M. J. , et al. (2015). Antarctic intermediate water properties since 400 ka recorded in infaunal

(*Uvigerina peregrina*) and epifaunal (*Planulina wuellerstorfi*) benthic foraminifera. *Earth and Planetary Science Letters*, 428(15), 193-203. https://doi.org/10.1016/j.epsl.2015.07.013

Fieux, M., C., Andrié, E., & Charriaud, et al. (1996). Hydrological and chlorofluoromethane measurements of the indonesian throughflow entering the indian ocean. *Journal of Geophysical Research Oceans*, 101(C5), 12433– 12454. https://doi.org/10.1029/96JC00207

Fu, X., Cohen, T. J., & Arnold, L. J. (2017). Extending the record of lacustrine phases beyond the last interglacial for Lake Eyre in central Australia using luminescence dating. *Quaternary Science Reviews*, 162, 88-110. http://dx.doi.org/10.1016/j.quascirev.2017.03.002

Gallagher, S.J., Wallace, M.W., Hoiles, P.W. & Southwood, J. M. 2014. Seismic and stratigraphic evidence for reef expansion and onset of aridity on the Northwest Shelf of Australia during the Pleistocene. *Marine and Petroleum Geology* v. 57, 470-481. 10.1016/j.marpetgeo.2014.06.011

Gallagher, S.J., Fulthorpe, C.S., Bogus, K., Auer, G., Baranwal, S., Castañeda, I.S., et al. (2017a). Site U1464. In Gallagher, S.J., Fulthorpe, C.S., Bogus, K., and the Expedition 356 Scientists, *Indonesian Throughflow*. Proceedings of the International Ocean Discovery Program, 356: College Station, TX (International Ocean Discovery Program). http://dx.doi.org/10.14379/iodp.proc.356.109.2017

Gallagher, S.J., Fulthorpe, C.S., Bogus, K., Auer, G., Baranwal, S., Castañeda, I.S., et al. (2017b). Site U1463. In Gallagher, S.J., Fulthorpe, C.S., Bogus, K., and the Expedition 356 Scientists, *Indonesian Throughflow*. Proceedings of the International Ocean Discovery Program, 356: College Station, TX (International Ocean Discovery Program). http://dx.doi.org/10.14379/iodp.proc.356.108.2017

Gallagher, S.J., Reuning, L., Himmler, T., Henderiks, J., De Vleeschouwer, D., Groeneveld, J., et al. (2018). The enigma of rare Quaternary oolites in the Indian and Pacific Oceans: a result of global oceanographic physicochemical conditions or a sampling bias. *Quaternary Science Reviews*, 200, 114-122. http://doi.org/10.1016/j.quascirev.2018.09.028

Gallagher, S.J. & deMenocal, P.B. (2019). Finding dry spells in Ocean Sediments. *Oceanography*, 32 (1), 38-41. https://doi.org/10.5670/oceanog.2019.120

Gallagher, S. J., & Wagstaff, B. E. (2021). Quaternary environments and monsoonal climate off northwest Australia: Palynological evidence from Ocean Drilling Program Site 765. *Quaternary Science Reviews*, 259, 106917. https://doi.org/10.1016/j.quascirev.2021.106917

Ganopolski, A., Rahmstorf, S., Petoukhov, V., & Claussen, M. (1998). Simulation of modern and glacial climates with a coupled global model of intermediate complexity. *Nature*, 391(6665), 351-356. https://doi.org/10.1038/34839

Grant, K. M., Amarathunga, U., Amies, J. D., Hu, P., Qian, Y., Penny, T., et al. (2022). Organic carbon burial in Mediterranean sapropels intensified during Green Sahara Periods since 3.2 Myr ago. *Communications Earth & Environment*, 3(1), 11. https://doi.org/10.1038/s43247-021-00339-9

Grinsted, A., Moore, J. C., & Jevrejeva, S. (2004). Application of the cross wavelet transform and wavelet coherence to geophysical time series. *Nonlinear Processes in Geophysics*, 11(5/6), 561-566. https://doi.org/10.5194/npg-11-561-2004

Groeneveld, J., De Vleeschouwer, D., McCaffrey, J. C., & Gallagher, S. J. (2021). Dating the northwest shelf of Australia since the Pliocene. *Geochemistry, Geophysics, Geosystems*, 22(3), e2020GC009418. https://doi.org/10.1029/2020GC009418

Hallenberger, M., Reuning, L., Gallagher, S. J., Back, S., Ishiwa, T., Christensen, B. A., & Bogus, K. (2019). Increased fluvial runoff terminated inorganic aragonite precipitation on the Northwest Shelf of Australia during the early Holocene. *Scientific Reports*, 9(1), 18356. https://doi.org/10.1038/s41598-019-54981-7

Hallenberger, M., Reuning, L., Back, S., Gallagher, S. J., Iwatani, H., & Lindhorst, K. (2022). Climate and sea-level controlling internal architecture of a Quaternary carbonate ramp (Northwest Shelf of Australia). *Sedimentology*, 69(3), 1276-1300. https://doi.org/10.1111/sed.12948

Hennekam, R., Grant, K. M., Rohling, E. J., Tjallingii, R., Heslop, D., Roberts, A. P., et al. (2022). Accurately calibrated XRF-CS record of Ti/Al reveals Early Pleistocene aridity/humidity variability over North Africa and its close relationship to low-latitude insolation. *Climate of the Past*, 18(11), 2509–2521. https://doi.org/10.5194/cp-18-2509-2022

Herbert, T.D. (1997). A long marine history of carbon cycle modulation by orbital-climatic changes. *Proceedings of the National Academy of Sciences of the United States of America*, 94 16, 8362-9. https://doi.org/10.1073/pnas.94.16.8362

Herraiz-Borreguero, L., & Rintoul, S. R. (2011). Subantarctic mode water: distribution and circulation. *Ocean Dynamics*, 61(1), 103-126. https://doi.org/10.1007/s10236-010-0352-9

Hesse, P. P., Magee, J. W., & van der Kaars, S. (2004). Late Quaternary climates of the Australian arid zone: a review. *Quaternary International*, 118, 87-102. https://doi.org/10.1016/S1040-6182(03)00132-0

Hinnov, L. A. (2000). New perspectives on orbitally forced stratigraphy. *Annual Review of Earth and Planetary Sciences*, 28(1), 419-475. https://doi.org/10.1146/annurev.earth.28.1.419

Holbourn, A., Kuhnt, W., Kawamura, H., Jian, Z., Grootes, P., Erlenkeuser, H., & Xu, J. (2005). Orbitally paced paleoproductivity variations in the Timor Sea and Indonesian Throughflow variability during the last 460 kyr. *Paleoceanography*, 20(3). https://doi.org/10.1029/2004PA001094

Holbourn, A.E., Kuhnt, W., Schulz, M., Flores, J., & Andersen, N. (2007). Orbitally-paced climate evolution during the middle Miocene "Monterey" carbon-isotope excursion. *Earth and Planetary Science Letters*, 261, 534-550. https://doi.org/10.1016/j.epsl.2007.07.026

Hovan, S. A., Rea, D. K., & Pisias, N. G. (1991). Late Pleistocene continental climate and oceanic variability recorded in northwest Pacific sediments. *Paleoceanography*, 6(3), 349-370. https://doi.org/10.1029/91PA00559

Imbrie, J., Hays, J.D., Martinson, D.B., McIntyre, A., Mix, A.C., Morlet, J.J., et al. (1984). The orbital theory of Pleistocene climate: support from a revised chronology of the marine $\delta^{18}O$ record. In: Berger, A., et al. (Eds.), *Milankovitch and Climate* (part 1, pp. 269–305). D. Reidel Publishing Company.

James, N. P., Bone, Y., Kyser, T. K., Dix, G. R., & Collins, L. B. (2004). The importance of changing oceanography in controlling late Quaternary carbonate sedimentation on a high-energy, tropical, oceanic ramp: north-western Australia. *Sedimentology*, 51(6), 1179-1205. https://doi.org/10.1111/j.1365-3091.2004.00666.x

James, N.P., Bone, Y., & Kyser, T.K. (2005). Where Has All the Aragonite Gone? Mineralogy of Holocene Neritic Cool-Water Carbonates, Southern Australia. *Journal of Sedimentary Research*, 75, 454-463. https://doi.org/10.2110/jsr.2005.035

Kalnay, E., Kanamitsu, M., Kistler, R., Collins, W., Deaven, D., Gandin, L., et al. (1996). The NCEP/NCAR 40-year reanalysis project. *Bulletin of the American Meteorological Society*, 77(3), 437-472. https://doi.org/10.1175/1520-0477(1996)077<0437:TNYRP>2.0.CO;2

Kershaw, A. P., van der Kaars, S., & Moss, P. T. (2003). Late Quaternary Milankovitch-scale climatic change and variability and its impact on monsoonal Australasia. *Marine Geology*, 201(1-3), 81-95. https://doi.org/10.1016/S0025-3227(03)00210-X

Key, R.M., Olsen, A., van Heuven, S., Lauvset, S. K., Velo, A., Lin, X., et al. (2015). *Global Ocean Data Analysis Project, Version 2 (GLODAPv2), ORNL/CDIAC-162, NDP-093*. Carbon Dioxide Information Analysis Center, Oak Ridge National Laboratory, US Department of Energy, Oak Ridge, Tennessee. https://doi.org/10.3334/CDIAC/OTG.NDP093_GLODAPv2

Kochhann, K. G., Holbourn, A., Kuhnt, W., Channell, J. E., Lyle, M., Shackford, J. K., et al. (2016). Eccentricity pacing of eastern equatorial Pacific carbonate dissolution cycles during the Miocene Climatic Optimum. *Paleoceanography*, 31(9), 1176-1192. https://doi.org/10.1002/2016PA002988

Kocken, I.J., Cramwinckel, M.J., Zeebe, R.E., Middelburg, J.J., & Sluijs, A. (2019). The 405 kyr and 2.4 Myr eccentricity components in Cenozoic carbon isotope records. *Climate of the Past*. https://doi.org/10.5194/cp-15-91-2019

Kuhnt, W., Holbourn, A., Xu, J., Opdyke, B., De Deckker, P., Röhl, U., & Mudelsee, M. (2015). Southern Hemisphere control on Australian monsoon variability during the late deglaciation and Holocene. *Nature Communications*, 6(1), 5916. https://doi.org/10.1038/ncomms6916

Larrasoaña, J. C., Roberts, A. P., Rohling, E. J., Winklhofer, M., & Wehausen, R. (2003). Three million years of monsoon variability over the northern Sahara. *Climate Dynamics*, 21(7-8), 689-698. https://doi.org/10.1007/s00382-003-0355-z

Laskar, J., Robutel, P., Joutel, F., Gastineau, M., Correia, A. C. M., & Levrard, B. (2004). A long-term numerical solution for the insolation quantities of the Earth. *Astronomy & Astrophysics*, 428(1), 261-285. https://doi.org/10.1051/0004-6361:20041335

Leuschner, D. C., & Sirocko, F. (2003). Orbital insolation forcing of the Indian Monsoon–a motor for global climate changes?. *Palaeogeography, Palaeoclimatology, Palaeoecology*, 197(1-2), 83-95. https://doi.org/10.1016/S0031-0182(03)00387-0

Lewis, E. & Wallace, D. W. R. (1998). Program Developed for CO2 System Calculations, ORNL/CDIAC-105, Carbon Dioxide Inf. Anal. Cent., Oak Ridge Natl. Lab., Oak Ridge, Tenn., 38 pp.

Liebrand, D., Beddow, H. M., Lourens, L. J., Pälike, H., Raffi, I., Bohaty, S. M., et al. (2016). Cyclostratigraphy and eccentricity tuning of the early Oligocene through early Miocene (30.1–

17.1 Ma): Cibicides mundulus stable oxygen and carbon isotope records from Walvis Ridge Site 1264. *Earth and Planetary Science Letters*, 450, 392-405. https://doi.org/10.1016/j.epsl.2016.06.007

Lisiecki, L.E., & Raymo, M.E. (2005). A Pliocene-Pleistocene stack of 57 globally distributed benthic δ18O records. *Paleoceanography*, 20, 1-17. https://doi.org/10.1029/2004PA001071

Liu, Y., Lo, L., Shi, Z., Wei, K. Y., Chou, C. J., Chen, Y. C., et al. (2015). Obliquity pacing of the western Pacific Intertropical Convergence Zone over the past 282,000 years. *Nature Communications*, 6(1), 1-7. https://doi.org/10.1038/ncomms10018

Ma, W., Tian, J., Li, Q., & Wang, P. (2011). Simulation of long eccentricity (400-kyr) cycle in ocean carbon reservoir during Miocene Climate Optimum: Weathering and nutrient response to orbital change. *Geophysical Research Letters*, 38. https://doi.org/10.1029/2011GL047680

Magee, J. W., Miller, G. H., Spooner, N. A., & Questiaux, D. (2004). Continuous 150 ky monsoon record from Lake Eyre, Australia: insolation-forcing implications and unexpected Holocene failure. *Geology*, 32(10), 885-888. https://doi.org/10.1130/G20672.1

Mantsis, D. F., Lintner, B. R., Broccoli, A. J., Erb, M. P., Clement, A. C., & Park, H. S. (2014). The response of large-scale circulation to obliquity-induced changes in meridional heating gradients. *Journal of Climate*, 27(14), 5504-5516. https://doi.org/10.1175/JCLI-D-13-00526.1

McClymont, E. L., Elmore, A. C., Kender, S., Leng, M. J., Greaves, M., & Elderfield, H. (2016). Pliocene-Pleistocene evolution of sea surface and intermediate water temperatures from the southwest Pacific. *Paleoceanography*, 31(6), 895-913. https://doi.org/10.1002/2016PA002954

McGowan, H., & Clark, A. (2008). Identification of dust transport pathways from Lake Eyre, Australia using Hysplit. *Atmospheric Environment*, 42(29), 6915-6925. https://doi.org/10.1016/j.atmosenv.2008.05.053

McTainsh, G. H. (1989). Quaternary aeolian dust processes and sediments in the Australian region. *Quaternary Science Reviews*, 8(3), 235-253. https://doi.org/10.1016/0277-3791(89)90039-5

Mélice, J. L., Coron, A., & Berger, A. (2001). Amplitude and frequency modulations of the Earth's obliquity for the last million years. *Journal of Climate*, 14(6), 1043-1054. https://doi.org/10.1175/1520-0442(2001)014<1043:AAFMOT>2.0.CO;2

Miller, G., Mangan, J., Pollard, D., Thompson, S., Felzer, B., & Magee, J. (2005). Sensitivity of the Australian Monsoon to insolation and vegetation: implications for human impact on continental moisture balance. *Geology*, 33(1), 65-68. https://doi.org/10.1130/G21033.1

Miller, G. H., Magee, J. W., Fogel, M. L., Wooller, M. J., Hesse, P. P., Spooner, N. A., et al. (2018). Wolfe Creek Crater: A continuous sediment fill in the Australian Arid Zone records changes in monsoon strength through the Late Quaternary. *Quaternary Science Reviews*, 199, 108-125. https://doi.org/10.1016/j.quascirev.2018.07.019

Moore Jr, T. C., Pisias, N. G., & Dunn, D. A. (1982). Carbonate time series of the Quaternary and late Miocene sediments in the Pacific Ocean: a spectral comparison. *Marine Geology*, 46(3-4), 217-233. https://doi.org/10.1016/0025-3227(82)90081-0

Mudelsee, M., & M. E. Raymo (2005). Slow dynamics of the Northern Hemisphere glaciation. *Paleoceanography*, 20, PA4022. https://doi.org/10.1029/2005PA001153

Pälike, H., Norris, R. D., Herrle, J. O., Wilson, P. A., Coxall, H. K., Lear, C. H., et al. (2006). The heartbeat of the Oligocene climate system. *Science*, 314(5807), 1894-1898. https://doi.org/10.1126/science.1133822

Pei, R., Kuhnt, W., Holbourn, A., Hingst, J., Koppe, M., Schultz, J., et al. (2021). Monitoring Australian Monsoon variability over the past four glacial cycles. *Palaeogeography, Palaeoclimatology, Palaeoecology*, 568, 110280. https://doi.org/10.1016/j.palaeo.2021.110280

Pisias, N. G., & Rea, D. K. (1988). Late Pleistocene paleoclimatology of the central equatorial Pacific: Sea surface response to the southeast trade winds. *Paleoceanography*, 3(1), 21-37. https://doi.org/10.1029/PA003i001p00021

Rayner, N. A. A., Parker, D. E., Horton, E. B., Folland, C. K., Alexander, L. V., Rowell, D. P., et al. (2003). Global analyses of sea surface temperature, sea ice, and night marine air temperature since the late nineteenth century. *Journal of Geophysical Research: Atmospheres*, 108(D14). https://doi.org/10.1029/2002JD002670

Reichart, G.-J. (1997). Late Quaternary variability of the Arabian Sea monsoon and oxygen minimum zone (Ph.D. thesis). Retrieved from http://dspace.library.uu.nl/handle/1874/274419. Netherlands: Utrecht University.

Reuning, L., Deik, H., Petrick, B., Auer, G., Takayanagi, H., Iryu, Y., et al. (2022). Contrasting intensity of aragonite dissolution and dolomite cementation in glacial versus interglacial

intervals of a subtropical carbonate succession. *Sedimentology*, 69. https://doi.org/10.1111/sed.12985

Rial, J. A. (1999). Pacemaking the ice ages by frequency modulation of Earth's orbital eccentricity. *Science*, 285(5427), 564-568. https://www.science.org/doi/10.1126/science.285.5427.564

Rial, J. A., & Anaclerio, C. A. (2000). Understanding nonlinear responses of the climate system to orbital forcing. *Quaternary Science Reviews*, 19(17-18), 1709-1722. https://doi.org/10.1016/S0277-3791(00)00087-1

Richardson, L. E., Middleton, J. F., Kyser, T. K., James, N. P., & Opdyke, B. N. (2019). Shallow water masses and their connectivity along the southern Australian continental margin. *Deep Sea Research Part I: Oceanographic Research Papers*, 152, 103083. https://doi.org/10.1016/j.dsr.2019.103083

Rickaby, R.E., Bard, E., Sonzogni, C., Rostek, F., Beaufort, L., Barker, S., et al. (2007). Coccolith chemistry reveals secular variations in the global ocean carbon cycle. *Earth and Planetary Science Letters*, 253, 83-95. https://doi.org/10.1016/j.epsl.2006.10.016

Ridgway, K. R. , & Godfrey, J. S. . (2015). The source of the Leeuwin Current seasonality. *Journal of Geophysical Research Oceans*, 120(10), 6843-6864. https://doi.org/10.1002/2015JC011049

Rohling, E. J., Yu, J., Heslop, D., Foster, G. L., Opdyke, B., & Roberts, A. P. (2021). Sea level and deep-sea temperature reconstructions suggest quasi-stable states and critical transitions over the past 40 million years. *Science Advances*, 7(26), eabf5326. https://doi.org/10.1126/sciadv.abf5326

Rosenthal, Y., Holbourn, A.E., Kulhanek, D.K., Aiello, I.W., Babila, T.L., Bayon, G., et al. (2018). Site U1482. In Rosenthal, Y., Holbourn, A.E., Kulhanek, D.K., and the Expedition 363 Scientists, Western Pacific Warm Pool. Proceedings of the International Ocean Discovery Program, 363: College Station, TX (International Ocean Discovery Program). https://doi.org/10.14379/iodp.proc.363.103.2018

Rothwell, R. G. & Croudace, I. W. (2015). Twenty years of XRF core scanning marine sediments: what do geochemical proxies tell us?. In *Micro-XRF Studies of Sediment Cores* (pp. 25-102). Springer, Dordrecht.

Santer, B. D., Wigley, T. M. L., Boyle, J. S., Gaffen, D. J., Hnilo, J. J., Nychka, D., et al. (2000). Statistical significance of trends and trend differences in layer-average atmospheric temperature time series. *Journal of Geophysical Research: Atmospheres*, 105(D6), 7337-7356. https://doi.org/10.1029/1999JD901105

Schneider, U., Becker, A., Finger, P., Meyer-Christoffer, A., Rudolf, B., & Ziese, M. (2011). GPCC Full Data Reanalysis Version 6.0 at 0.5°: Monthly Land-Surface Precipitation from Rain-Gauges built on GTS-based and Historic Data. https://doi.org/10.5676/DWD_GPCC/FD_M_V7_050

Schulte, S., & Bard, E. (2003). Past changes in biologically mediated dissolution of calcite above the chemical lysocline recorded in Indian Ocean sediments. *Quaternary Science Reviews*, 22, 1757-1770. https://doi.org/10.1016/S0277-3791(03)00172-0

Schulz, M., & Mudelsee, M. (2002). REDFIT: estimating red-noise spectra directly from unevenly spaced paleoclimatic time series. *Computers & Geosciences*, 28(3), 421-426. https://doi.org/10.1016/S0098-3004(01)00044-9

Schwendike, J., Govekar, P., Reeder, M. J., Wardle, R., Berry, G. J., & Jakob, C. (2014). Local partitioning of the overturning circulation in the tropics and the connection to the Hadley and Walker circulations. *Journal of Geophysical Research: Atmospheres*, 119(3), 1322-1339. https://doi.org/10.1002/2013JD020742

Sexton, P.F., & Barker, S. (2012). Onset of 'Pacific-style' deep-sea sedimentary carbonate cycles at the mid-Pleistocene transition. *Earth and Planetary Science Letters*, 321, 81-94. https://doi.org/10.1016/j.epsl.2011.12.043

Shi, Z. G., Liu, X. D., Sun, Y. B., An, Z. S., Liu, Z., & Kutzbach, J. (2011). Distinct responses of East Asian summer and winter monsoons to astronomical forcing. *Climate of the Past*, 7(4), 1363-1370. https://doi.org/10.5194/cp-7-1363-2011

Strong, C. L., Parsons, K., McTainsh, G. H., & Sheehan, A. (2011). Dust transporting wind systems in the lower Lake Eyre Basin, Australia: A preliminary study. *Aeolian Research*, 2(4), 205-214. https://doi.org/10.1016/j.aeolia.2010.11.001

Stuut, J. B. W., Temmesfeld, F., & De Deckker, P. (2014). A 550 ka record of aeolian activity near North West Cape, Australia: inferences from grain-size distributions and bulk chemistry of SE Indian Ocean deep-sea sediments. *Quaternary Science Reviews*, 83, 83-94. https://doi.org/10.1016/j.quascirev.2013.11.003

Stuut, J. B. W., De Deckker, P., Saavedra-Pellitero, M., Bassinot, F., Drury, A. J., Walczak, M. H., et al. (2019). A 5.3-million-year history of monsoonal precipitation in northwestern Australia. *Geophysical Research Letters*, 46(12), 6946-6954. https://doi.org/10.1029/2019GL083035

Sulpis, O., Jeansson, E., Dinauer, A., Lauvset, S.K., & Middelburg, J.J. (2021). Calcium carbonate dissolution patterns in the ocean. *Nature Geoscience*, 14, 423 - 428. https://doi.org/10.1038/s41561-021-00743-y

Sun, Y., Clemens, S. C., An, Z., & Yu, Z. (2006). Astronomical timescale and palaeoclimatic implication of stacked 3.6-Myr monsoon records from the Chinese Loess Plateau. *Quaternary Science Reviews*, 25(1-2), 33-48. https://doi.org/10.1016/j.quascirev.2005.07.005

Suppiah, R. (1992). The Australian summer monsoon: A review. *Progress in Physical Geography*, 16(3), 283-318. https://doi.org/10.1177/030913339201600302

Suppiah, R., & Wu, X. (1998). Surges, cross-equatorial flows and their links with the Australian summer monsoon circulation and rainfall. *Australian Meteorological Magazine* 47, 113-130.

Talley, L. D., & Sprintall, J. (2005). Deep expression of the Indonesian Throughflow: Indonesian intermediate water in the South Equatorial Current. *Journal of Geophysical Research: Oceans*, 110(C10). https://doi.org/10.1029/2004JC002826

Taylor, J.R. (1997). *Introduction to Error Analysis, the Study of Uncertainties in Physical Measurements, 2nd Edition*. Sausalito, California: University Science Books.

Thompson, P. R., Bé, A. W., Duplessy, J. C., & Shackleton, N. J. (1979). Disappearance of pink-pigmented Globigerinoides ruber at 120,000 yr BP in the Indian and Pacific Oceans. *Nature*, 280(5723), 554-558. https://doi.org/10.1038/280554a0

Thomson, D. J. (1982). Spectrum estimation and harmonic analysis. *Proceedings of the IEEE*, 70(9), 1055-1096. https://doi.org/10.1109/PROC.1982.12433

Verosub, K. L., & Roberts, A. P. (1995). Environmental magnetism: Past, present, and future. *Journal of Geophysical Research: Solid Earth*, 100(B2), 2175-2192. https://doi.org/10.1029/94JB02713

Wade, B. S., Pearson, P. N., Berggren, W. A., & Pälike, H. (2011). Review and revision of Cenozoic tropical planktonic foraminiferal biostratigraphy and calibration to the geomagnetic polarity and astronomical time scale. *Earth-Science Reviews*, 104(1-3), 111-142. https://doi.org/10.1016/j.earscirev.2010.09.003

Wang, P., Tian, J., & Lourens, L. J. (2010). Obscuring of long eccentricity cyclicity in Pleistocene oceanic carbon isotope records. *Earth and Planetary Science Letters*, 290(3-4), 319-330. https://doi.org/10.1016/j.epsl.2009.12.028

Weltje, G. J., Bloemsma, M. R., Tjallingii, R., Heslop, D., Röhl, U., & Croudace, I. W. (2015). Prediction of geochemical composition from XRF core scanner data: a new multivariate approach including automatic selection of calibration samples and quantification of uncertainties. In *Micro-XRF Studies of Sediment Cores* (pp. 507-534). Springer, Dordrecht.

Westerhold, T., Röhl, U., Donner, B., McCarren, H.K., & Zachos, J.C. (2011). A complete high-resolution Paleocene benthic stable isotope record for the central Pacific (ODP Site 1209). *Paleoceanography*, 26. https://doi.org/10.1029/2010PA002092

Wijeratne, S., Pattiaratchi, C., & Proctor, R. (2018). Estimates of surface and subsurface boundary current transport around Australia. *Journal of Geophysical Research: Oceans*, 123(5), 3444-3466. https://doi.org/10.1029/2017JC013221

Wong, A. P. (2005). Subantarctic mode water and Antarctic intermediate water in the south Indian Ocean based on profiling float data 2000–2004. *Journal of Marine Research*, 63(4), 789-812. https://elischolar.library.yale.edu/journal_of_marine_research/101

Woo, M., & Pattiaratchi, C. (2008). Hydrography and water masses off the western Australian coast. *Deep Sea Research Part I: Oceanographic Research Papers*, 55(9), 1090-1104. https://doi.org/10.1016/j.dsr.2008.05.005

Woodruff, F., and Savin S. (1991). Mid-Miocene isotope stratigraphy in the deep sea: High-resolution correlations, paleoclimatic cycles, and sediment preservation. *Paleoceanography*, 6(6), 755–806. https://doi.org/10.1029/91PA02561

Wyrwoll, K. H., & Valdes, P. (2003). Insolation forcing of the Australian monsoon as controls of Pleistocene mega-lake events. *Geophysical Research Letters*, 30(24). https://doi.org/10.1029/2003GL018486

Wyrwoll, K. H., Liu, Z., Chen, G., Kutzbach, J. E., & Liu, X. (2007). Sensitivity of the Australian summer monsoon to tilt and precession forcing. *Quaternary Science Reviews*, 26(25-28), 3043-3057. https://doi.org/10.1016/j.quascirev.2007.06.026

Zeebe, R.E., Westerhold, T., Littler, K., & Zachos, J.C. (2017). Orbital forcing of the Paleocene and Eocene carbon cycle. *Paleoceanography*, 32, 440-465. https://doi.org/10.1002/2016PA003054

Zenk, W., Siedler, G., Ishida, A., Holfort, J., Kashino, Y., Kuroda, Y., et al. (2005). Pathways and variability of the Antarctic Intermediate Water in the western equatorial Pacific Ocean. *Progress in Oceanography*, 67(1-2), 245-281. https://doi.org/10.1016/j.pocean.2005.05.003

Zhang, P., Xu, J., Holbourn, A., Kuhnt, W., Beil, S., Li, T., et al. (2020). Indo-Pacific Hydroclimate in Response to Changes of the Intertropical Convergence Zone: Discrepancy on Precession and Obliquity Bands Over the Last 410 kyr. *Journal of Geophysical Research: Atmospheres*, 125(14), e2019JD032125. https://doi.org/10.1029/2019JD032125

Zhang, P., Xu, J., Holbourn, A., Kuhnt, W., Xiong, Z., & Li, T. (2022). Obliquity induced latitudinal migration of the Intertropical Convergence Zone during the past ~410 kyr. *Geophysical Research Letters*, 49(21), e2022GL100039. https://doi.org/10.1029/2022GL100039

Zhao, S., & Grant, K. (2024). Data for "Early Pleistocene orbital-scale variability in Australian Northwest Shelf sediments" submitted to Paleoceanography and Paleoclimatology [Data set]. Zenodo. https://doi.org/10.5281/zenodo.13286259

Zhao, S., Grant, K.M., Opdyke, B., Troitzsch, U., & Williams, I.S. (2024). Diagenetic dolomite in planktonic foraminifera on the Australian Northwest Shelf. *Sedimentology*. https://doi.org/10.1111/sed.13191

Ziveri, P., Gray, W.R., Anglada-Ortiz, G., Manno, C., Grelaud, M., Incarbona, A., et al. (2023). Pelagic calcium carbonate production and shallow dissolution in the North Pacific Ocean. *Nature Communications*, 14. https://doi.org/10.1038/s41467-023-36177-w

Figure 1. Precipitation (land), sea surface temperature (SST, ocean) and 850 hPa wind patterns of the Australian-Indonesian region for average austral summer (DJFM, top) and winter (JJAS, bottom). Precipitation data (1901-2013) is from the GPCC dataset (Schneider et al., 2011); SST data (1870-2017) is from the HadISST1 dataset (Rayner et al., 2003); Wind data (1948-2017) is from the NCEP/NCAR Reanalysis (Kalnay et al., 1996). Brown dash lines denote the Pilbara heat low (Suppiah, 1992). Red star marks IODP Site U1464 (this study). Core sites discussed in this study are indicated with black circles: IODP Site U1482 (Chen et al., 2022), IODP Site U1463 (Christensen et al., 2017), ODP Site 762 (Stuut et al., 2019), and DSDP Site 593 (McClymont et al., 2016). Detailed drainage basins (number 1-16) in the black rectangle are shown in Figure S1.

Figure 2. Bacon age-depth models for IODP Site U1464 (red). (a) Bacon age-depth model based on biostratigraphic ages. Black, blue, green, yellow and white dotted lines indicate the model's 99.99%, 99%, 95%, 90% and 80% probability intervals, respectively. (b) Refined Bacon age-depth model based on all biostratigraphic ages and tunings. Gradual darker grey shadings indicate the model's 99.99%, 99%, 95%, 90% and 80% probability intervals, respectively. Red line is the median probability. Red solid circles are biostratigraphic age control-points (Table S3).

Blue solid circles are four tie-points between eccentricity and the $CaCO_3$ record (Table S5). Yellow solid circles are 32 tie-points between obliquity and the filtered Log(Zr/Rb) record (Table S5). Black solid circle is the last occurrence of *G. ruber* (pink).

Figure 3. IODP Site U1464 bulk geochemistry from ~1.6 to 2.9 Ma. (a) $CaCO_3$; (b) Sr; (c) Fe; (d) Ti; (e) Rb and (f) Zr. Note that (a-d) show calibrated element concentrations, and (e, f) show scanning-XRF element counts. Bold lines (grey lines) in a-f are 21-point running averages (original data).

Figure 4. IODP Site U1464 eccentricity tuning. (a) Site U1464 $CaCO_3$ (gray: original time-series; purple: 21-point running average) on initial Bacon age model. (b) Eccentricity (green, Laskar et al., 2004). (c) Eccentricity (green) and Site U1464 $CaCO_3$ (gray: original time-series; purple: 21-point running average) rescaled after eccentricity tuning. Tie-points are indicated (dotted lines) for visual clarity. Cycle numbers represent 400 kyr eccentricity cycles, counted back from the present. ($CaCO_3$ y-axes are reversed for visual comparison).

Figure 5. IODP Site U1464 obliquity tuning. (a) Site U1464 Log(Zr/Rb) (gray: original time-series; green: 21-point running average) and its 0.023-0.027 band-pass filter (magenta) on the eccentricity tuning age model. (b) Obliquity (black, Laskar et al., 2004). (c) Obliquity (black) and the 0.023-0.027 band-pass filter (magenta) after obliquity tuning. 32 ties between obliquity minima and minima in the 0.023-0.027 filtered Log(Zr/Rb) are indicated (dotted lines) for visualization. Red triangles in (a) represent four eccentricity tuning tie-points.

Figure 6. IODP Site U1464 carbonate content and regional carbonate and benthic $\delta^{13}C$ records. (a) Site U1464 $CaCO_3$ (purple) and IODP Site U1482 $CaCO_3$ (blue dot, Rosenthal et al., 2018). (b) Site U1464 $CaCO_3$ (purple) and IODP Site U1482 *P. wuellerstorfi* $\delta^{13}C$ (blue, Chen et al., 2022). (c) Site U1464 $CaCO_3$ (purple) and IODP Site U1463 *Uvigerina spp.* $\delta^{13}C$ (green, Groeneveld et al., 2021). (d) Site U1464 $CaCO_3$ (purple) and DSDP Site 593 *P. wuellerstorfi* $\delta^{13}C$ (cyan, McClymont et al., 2016). The eccentricity tuning is used for the age model of Site U1464 $CaCO_3$ to validate the ~400 kyr eccentricity tuning. Red triangles represent four eccentricity tuning tie-points for Site U1464 $CaCO_3$. Blue (in a and b), green (in c) and cyan (in d) triangles represent age constraints for Site U1482 $CaCO_3$, *P. wuellerstorfi* $\delta^{13}C$, Site U1463 *Uvigerina spp.* $\delta^{13}C$ and Site 593 *P. wuellerstorfi* $\delta^{13}C$, respectively. It should be noted that the benthic $\delta^{13}C$ discrepancy between U1463 and U1482 (in b and c) may be attributed to different benthic foraminiferal species and diagenetic carbonates (Zhao et al., 2024).

Figure 7. Dust proxy records from the Australian NWS. $CaCO_3$-free $IRM_{1T@AF\ 170mT}$ (a, red), Log(Zr/Rb) (b, green: 21-point running average), and Log(Zr/Fe) (c, blue: 21-point running average) records at Site U1464. Wireline-derived Th/K record at Site U1463 (d, Christensen et al., 2017) and Log(Zr/Fe) record at Site ODP762 on Auer et al. (2020)'s updated age scale (e, orange: 9-point running average, Stuut et al., 2019). Dust maxima events are indicated in dash lines for visual alignment.

Figure 8. Comparison of Northwest Australian dust flux with global sea level, EAWM and SITIG from 1.6 to 2.9 Ma. (a) Site U1464 Log(Zr/Rb) and global sea level (Rohling et al., 2021) and (b) their cross wavelet spectrum. (c) Site U1464 Log(Zr/Rb) and a stacked MGSQ record (Sun et al., 2006) and (d) their cross wavelet spectrum. (e) Site U1464 Log(Zr/Rb) and the SITIG summer half-year (Laskar et al., 2004) and (f) their cross wavelet spectrum. The

30° N-30° S SITIG is shown in e (black) and the 0.023-0.027 filter of Log(Zr/Rb) is also shown in e (red line). In b, d and f, the cone of influence and 5% significance level are indicated by opaque shading and bold black contours, respectively. Arrows pointing to the right indicate an in-phase relationship.

Figure 1.

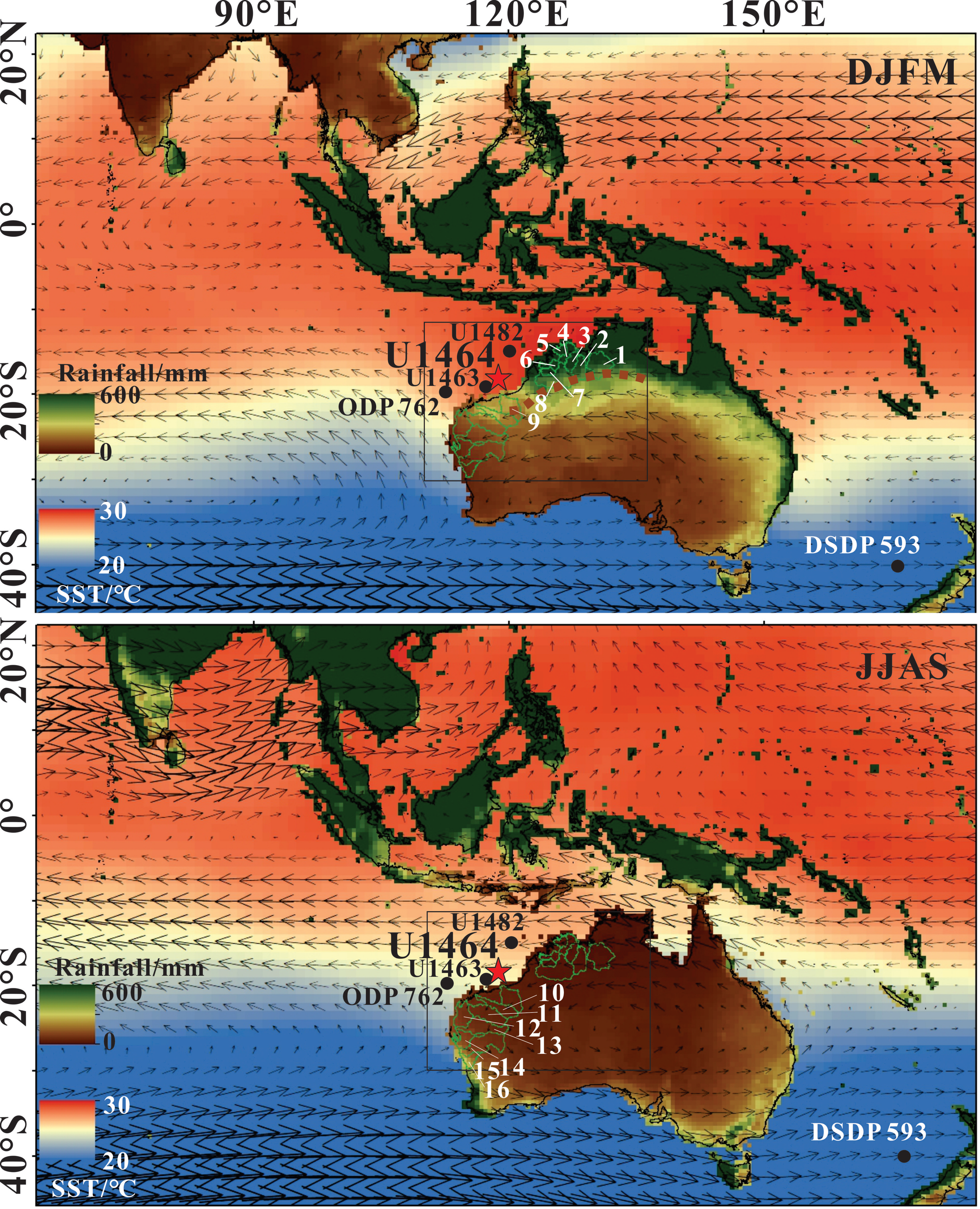
90°E
120°E
150°E
20°N
0°
20°S
40°S
DJFM
U1482
U1464
U1463
ODP 762
DSDP 593
1
2
3
4
5
6
7
8
9
Rainfall/mm
600
0
30
20
SST/°C
JJAS
U1482
U1464
U1463
ODP 762
DSDP 593
10
11
12
13
14
15
16
Rainfall/mm
600
0
30
20
SST/°C

Figure 2.

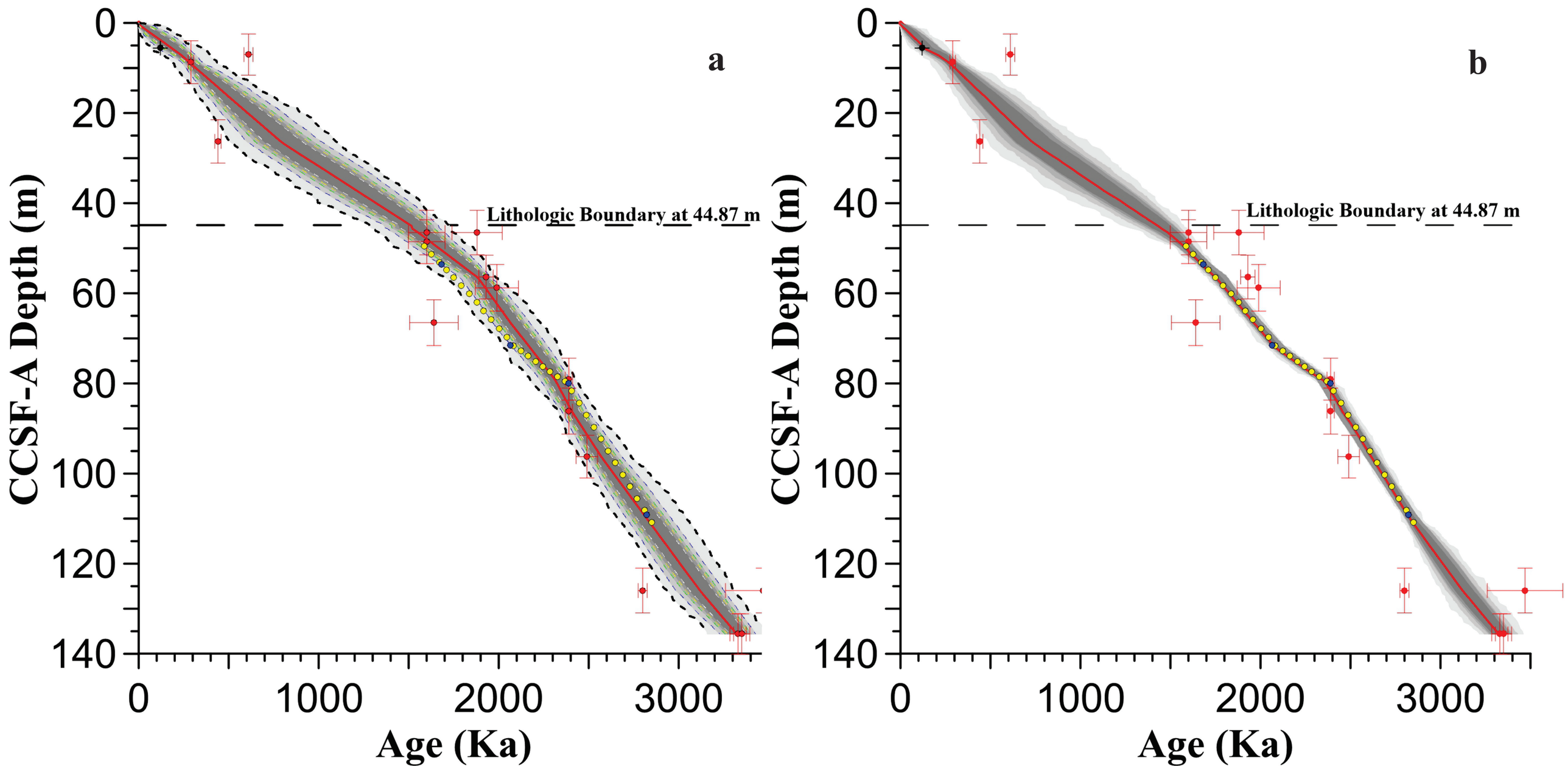
a
b
Lithologic Boundary at 44.87 m
Lithologic Boundary at 44.87 m
CCSF-A Depth (m)
CCSF-A Depth (m)
Age (Ka)
Age (Ka)
0
20
40
60
80
100
120
140
0
1000
2000
3000

Figure 3.

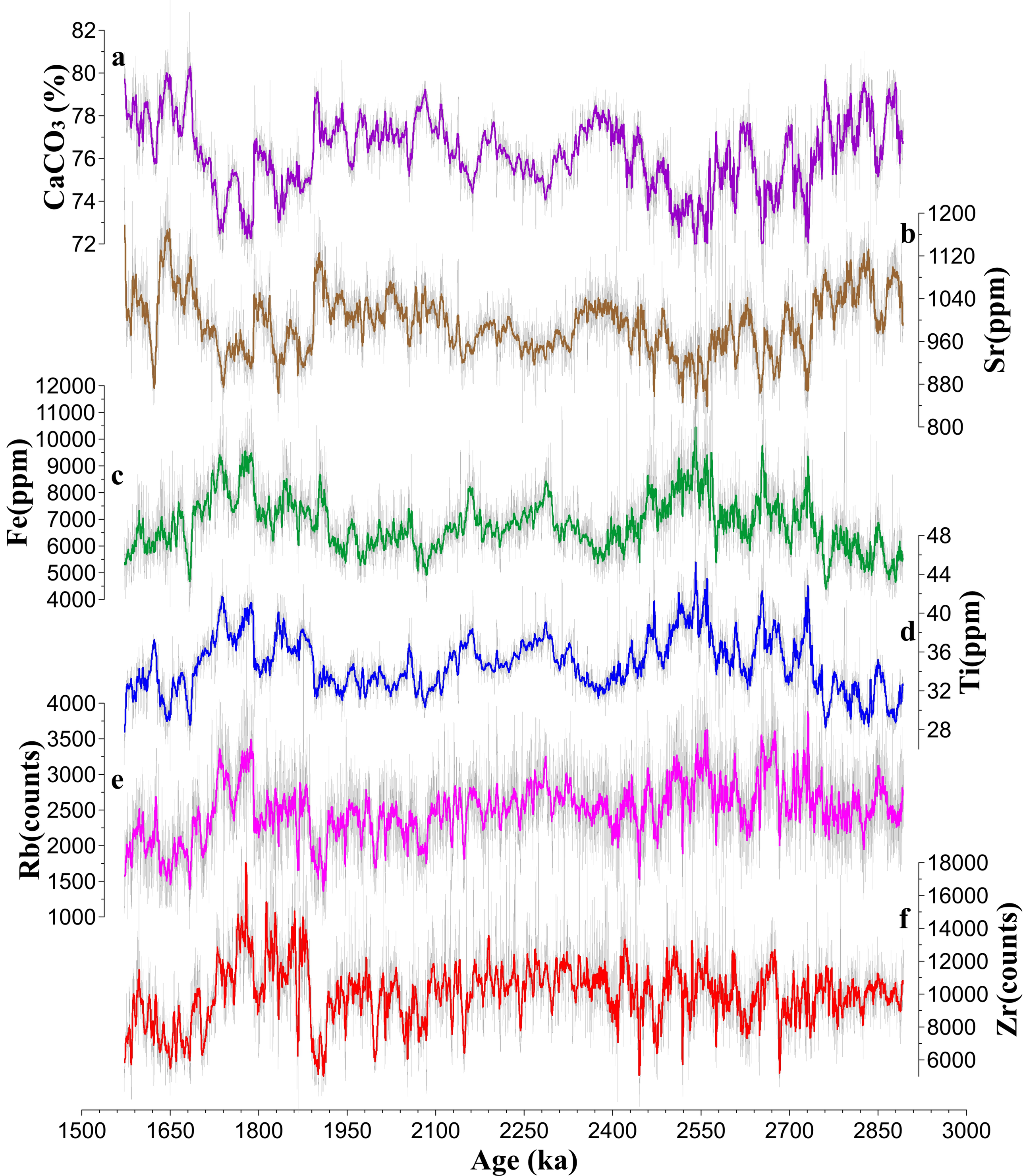
a
CaCO3 (%)
82
80
78
76
74
72
b
Sr(ppm)
1200
1120
1040
960
880
800
c
Fe(ppm)
12000
11000
10000
9000
8000
7000
6000
5000
4000
d
Ti(ppm)
48
44
40
36
32
28
e
Rb(counts)
4000
3500
3000
2500
2000
1500
1000
f
Zr(counts)
18000
16000
14000
12000
10000
8000
6000
1500
1650
1800
1950
2100
2250
2400
2550
2700
2850
3000
Age (ka)

Figure 4.

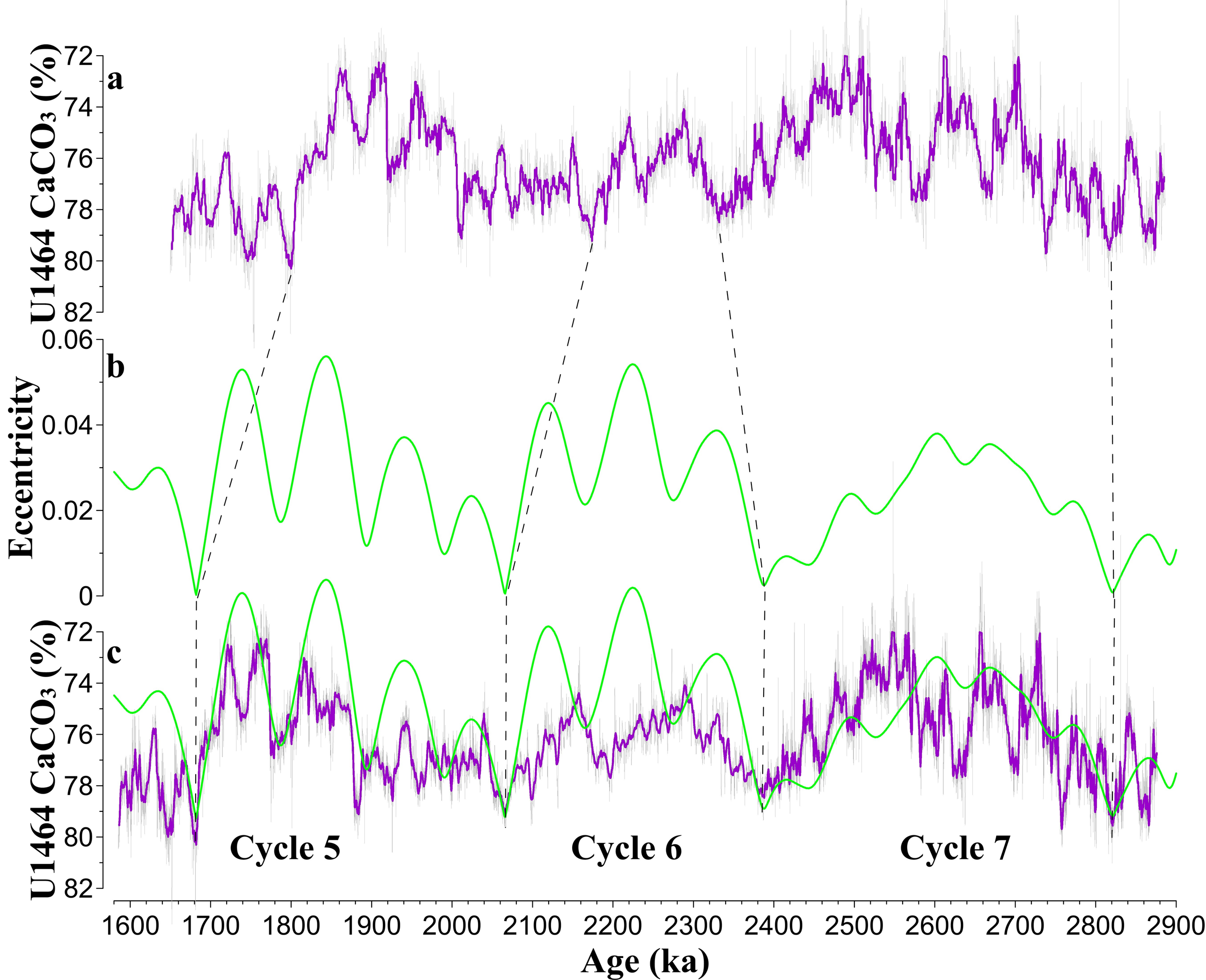
a
b
c
U1464 CaCO3 (%)
Eccentricity
U1464 CaCO3 (%)
72
74
76
78
80
82
0.06
0.04
0.02
0
Cycle 5
Cycle 6
Cycle 7
1600
1700
1800
1900
2000
2100
2200
2300
2400
2500
2600
2700
2800
2900
Age (ka)

Figure 5.

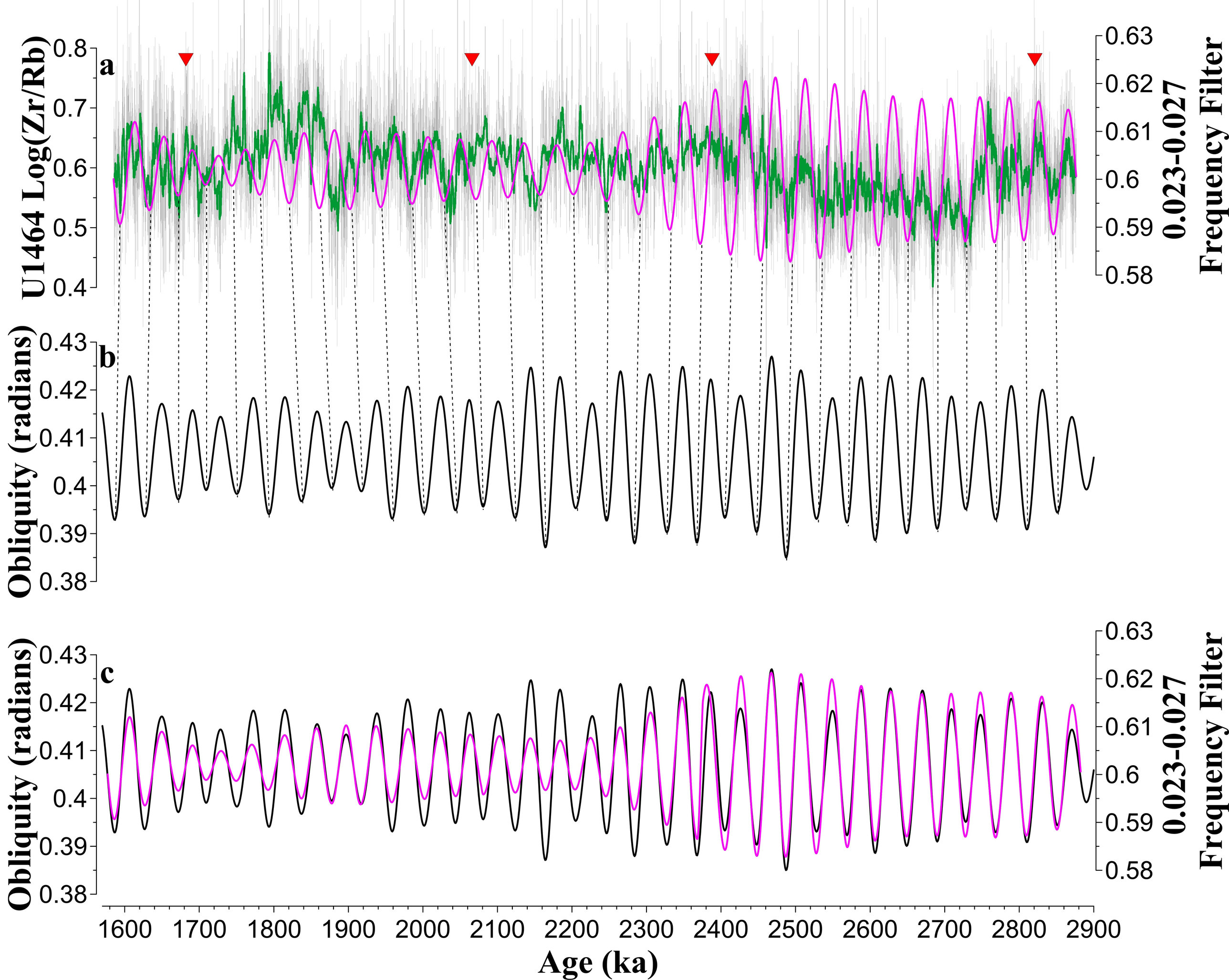
a
U1464 Log(Zr/Rb)
0.8
0.7
0.6
0.5
0.4
0.63
0.62
0.61
0.6
0.59
0.58
0.023-0.027
Frequency Filter
b
Obliquity (radians)
0.43
0.42
0.41
0.4
0.39
0.38
c
Obliquity (radians)
0.43
0.42
0.41
0.4
0.39
0.38
0.63
0.62
0.61
0.6
0.59
0.58
0.023-0.027
Frequency Filter
1600
1700
1800
1900
2000
2100
2200
2300
2400
2500
2600
2700
2800
2900
Age (ka)

Figure 6.

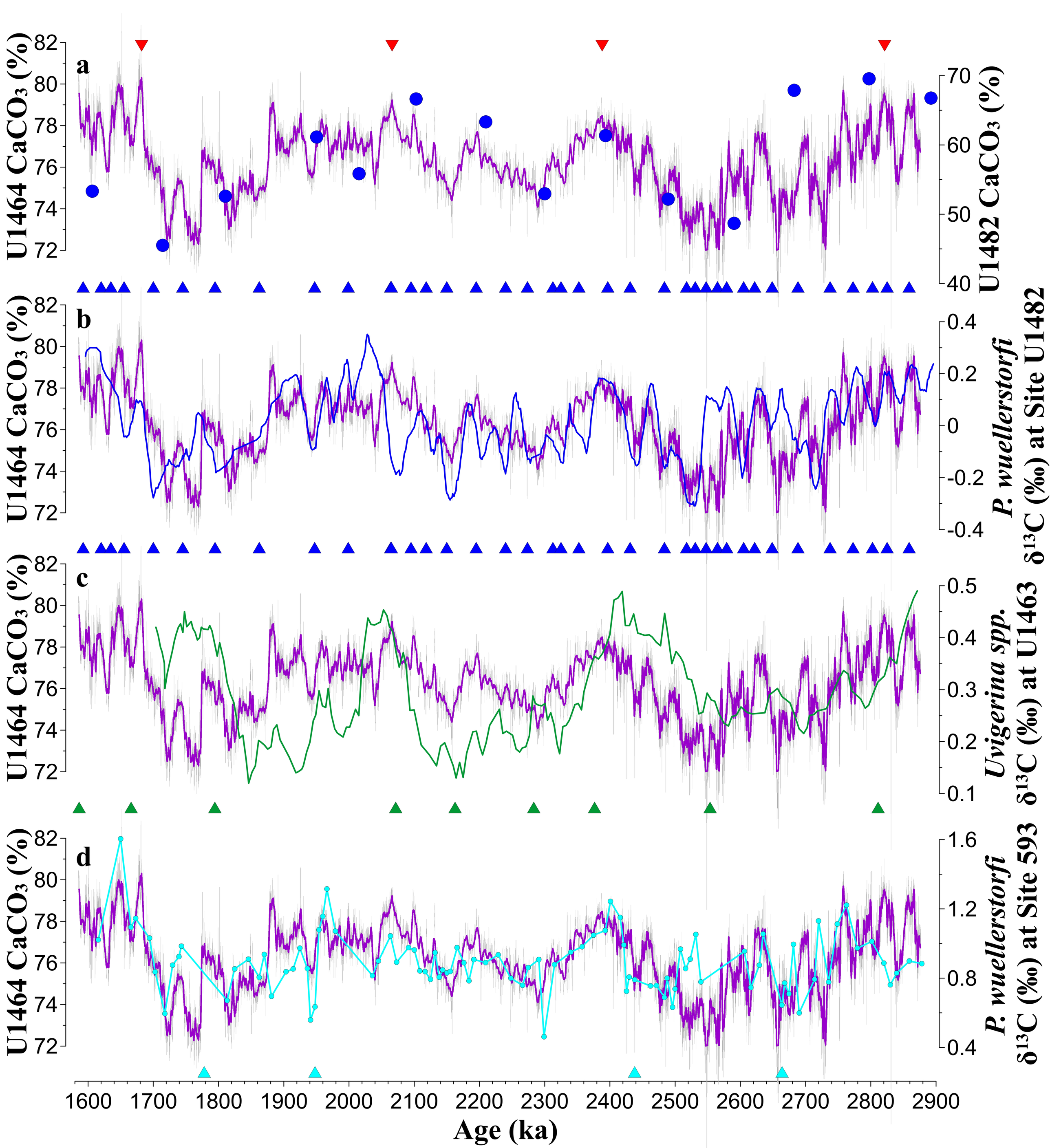
a
b
c
d
U1464 CaCO3 (%)
U1482 CaCO3 (%)
P. wuellerstorfi δ13C (‰) at Site U1482
Uvigerina spp. δ13C (‰) at U1463
P. wuellerstorfi δ13C (‰) at Site 593
Age (ka)

Figure 7.

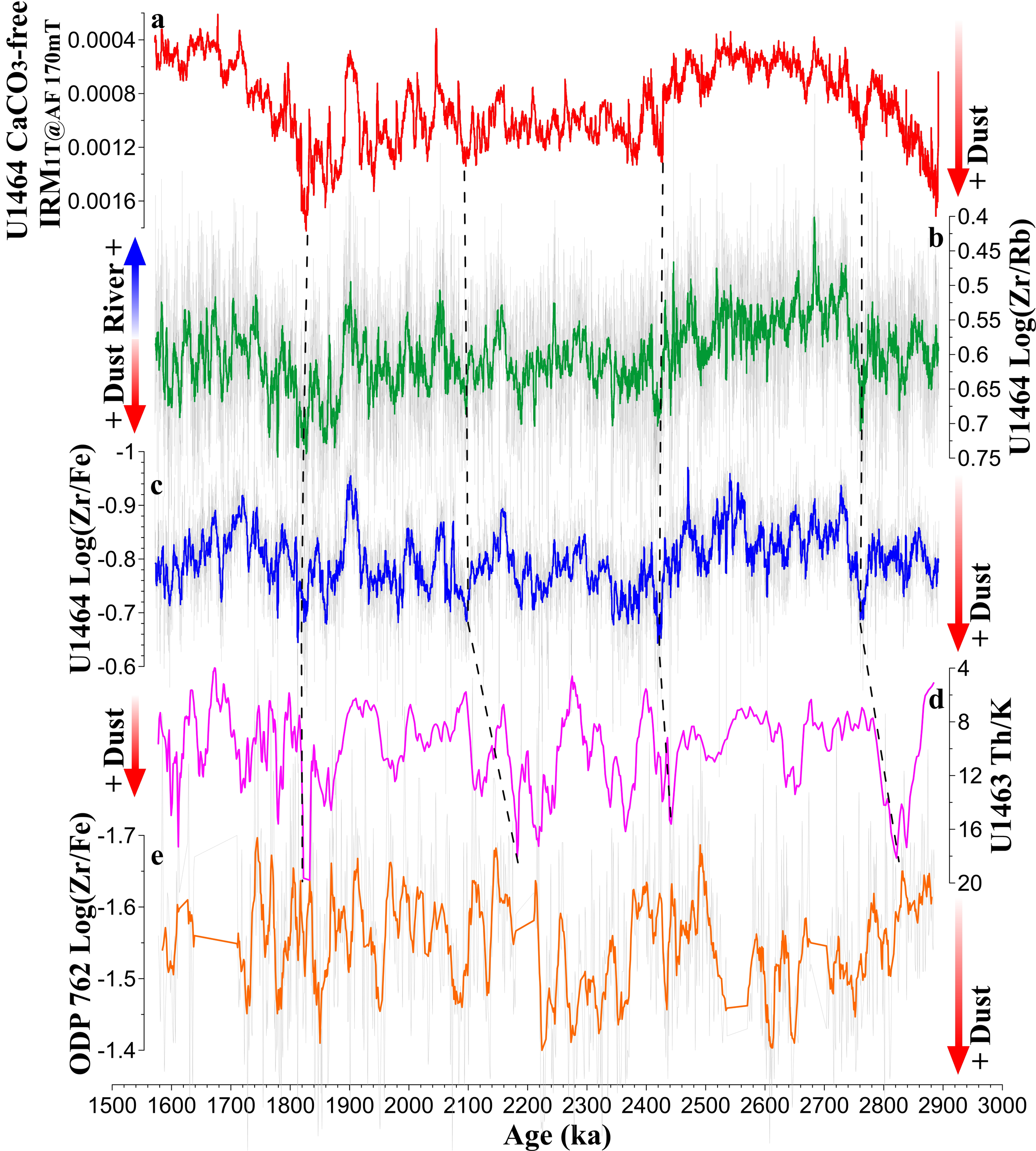
U1464 CaCO3-free
IRM1T@AF 170mT
0.0004
0.0008
0.0012
0.0016
a
+ Dust
+ Dust River +
b
0.4
0.45
0.5
0.55
0.6
0.65
0.7
0.75
U1464 Log(Zr/Rb)
U1464 Log(Zr/Fe)
-1
-0.9
-0.8
-0.7
-0.6
c
+ Dust
+ Dust
d
4
8
12
16
20
U1463 Th/K
ODP 762 Log(Zr/Fe)
-1.7
-1.6
-1.5
-1.4
e
+ Dust
1500 1600 1700 1800 1900 2000 2100 2200 2300 2400 2500 2600 2700 2800 2900 3000
Age (ka)

Figure 8.

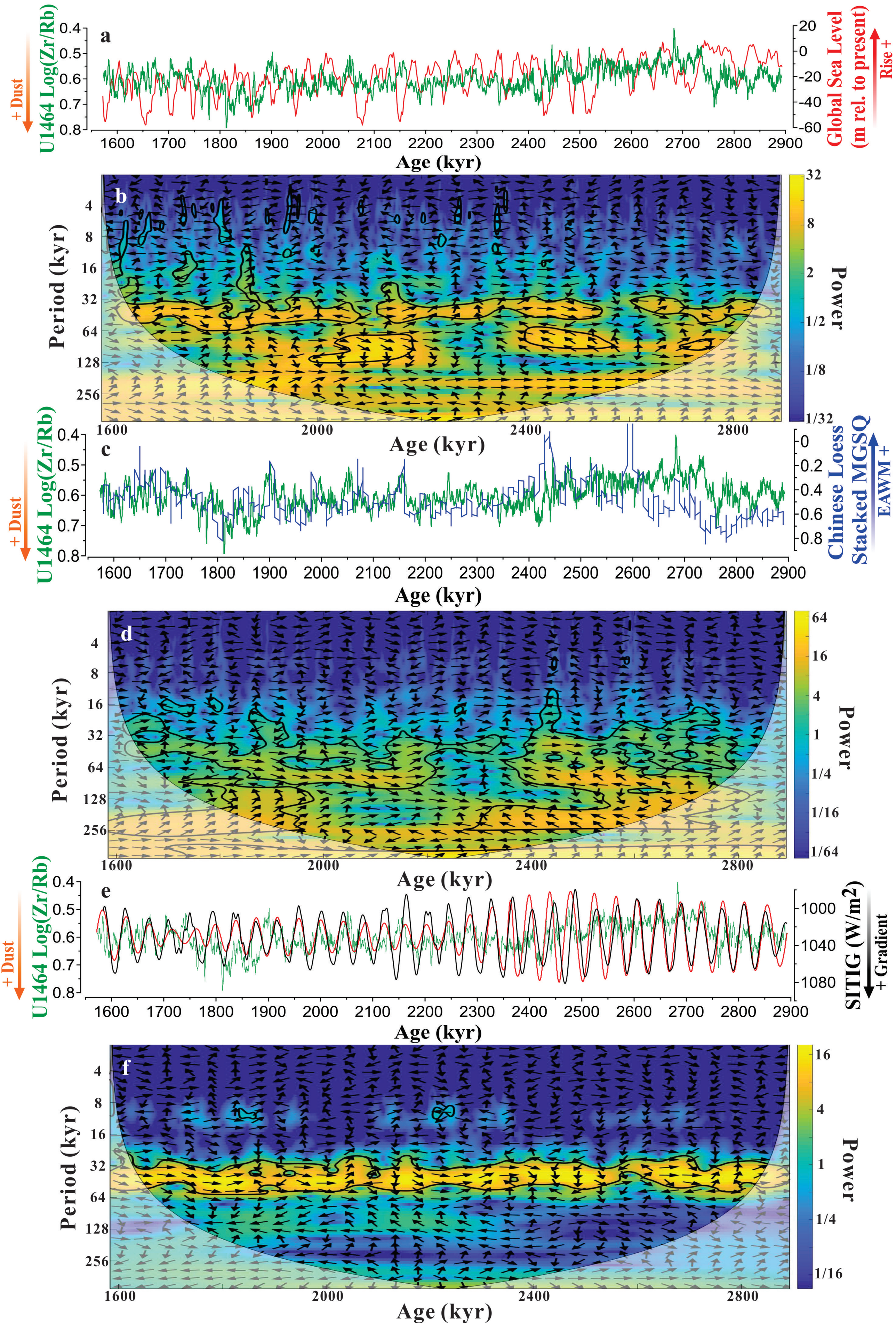
a
U1464 Log(Zr/Rb)
+ Dust
Global Sea Level (m rel. to present)
Rise +
Age (kyr)
b
Period (kyr)
Power
c
Chinese Loess
Stacked MGSQ
EAWM +
d
e
SITIG (W/m2)
+ Gradient
f